

Resilient Quantum Electron Microscopy

Hiroshi Okamoto¹

¹Department of Intelligent Mechatronics, Akita Prefectural University, Yurihonjo 015-0055, Japan

(Dated: April 2, 2020)

Shot-noise currently limits the resolution of electron cryomicroscopy of beam-sensitive biological specimens. Quantum metrology, despite the potential to surpass this limit, is notoriously sensitive to decoherence. We show that it is possible to significantly neutralize the adverse effect of inelastic electron scattering. This could allow us to study thick specimens of real biological interest.

The resolution of biological electron cryomicroscopy (cryoEM), unlike its light optical counterpart, is manifestly limited by shot noise. This is due to the small number of imaging electrons intended for avoiding radiation damage to the frozen specimen [1]. In single particle analysis (SPA) aiming at molecular modeling, the tolerable electron fluence, i.e. the number of electrons per unit area, ranges from the typical value of $(1 \sim 2) \times 10^3/\text{nm}^2$ up to $\sim 5 \times 10^3/\text{nm}^2$ [2]. On the other hand, biological objects consist of light elements, scatter electrons weakly, and are weak phase objects. Hence shot noise tends to bury the signal and thus limits the attainable resolution.

Quantum metrology, where phase measurement is a standard problem, is a natural approach to improving cryoEM. Recall that measuring a small phase θ with precision $\delta\theta$ takes $N \simeq \delta\theta^{-2}$ electrons because of the shot noise limit. There have recently been proposals of quantum electron microscopy (QEM) schemes that seek to approach the Heisenberg limit, where $N \simeq \delta\theta^{-1}$. These proposals are based on either repeated use of single electrons [3–10], or the use of entanglement between electrons and superconducting qubits [11–13]. Both methods accumulate the small phase θ onto a quantum object k times, resulting in a phase $k\theta$ after k electron-passing events through the specimen, which is then measured. Call k the repetition number. This is equivalent to measuring a hypothetical object with associated phase shift $k\theta$, using hypothetical N/k probe particles at the shot noise limit. As a result, we obtain an increased effective number of electrons as $kN \simeq \delta\theta^{-2}$, which approaches the Heisenberg limit at $k = N$.

In this work, we seek *universal* limits of biological QEM arising from electron-specimen interaction rather than limits pertaining to particular QEM schemes. Hence, besides the ability to pass the electron through the specimen, we assume full capability to initialize, manipulate, and measure the combined system comprising electrons and other quantum objects (i.e. qubits, without loss of generality). While any sufficiently versatile QEM scheme should be able to do this in principle, to be specific we present the results in terms of superconducting entanglement-enhanced QEM because of its versatility or even universality [14]. Naturally, we assume perfect electron lenses, electron detectors, qubits etc. Although the limit described below may not be the ultimate limit, our work extends any previously known limit of QEM. Henceforth any plane conjugate to the specimen plane is

referred to as an *image plane*, while any plane conjugate to the back focal plane of the objective lens is referred to as a *diffraction plane*.

The *raw* resolution of current cryoEM is about 3–5 nm [15]. All high resolution data to date are obtained only by averaging over at least tens of thousands of molecules of the same structure, by using e.g. SPA. This leaves much to be desired because the biologist would ultimately want to see single molecules or their complexes in their cellular context, rather than as ensemble average of purified molecules. We focus on unique, single specimens in the present work. At present, we can identify only very large proteins (\sim MDa) in the crowded cellular environment in electron cryotomography (ECT) [16]. Better resolutions would allow us to identify smaller proteins, or see protein structures such as α -helices and β -sheets at $0.5 \sim 1$ nm resolution [17], or model molecular structures at 0.3 nm resolution [18]. Although a recent study [19] shows that SPA works well with $\simeq 100$ keV electrons, it remains true that higher energy electrons are desirable in ECT to ensure transmission of electrons especially when the specimen is tilted. Moreover, since the *effective* thickness of the specimen is k times the actual thickness in QEM, we focus on 300 keV electrons hereafter.

The specimen thickness t is an important parameter in QEM. As quantum measurement is limited by lossy events, a relevant length to be compared with t is the inelastic mean free path $\Lambda = 200 - 350$ nm for 300 keV electrons [20]. Suppose, for now, that *all* inelastic scattering destroy quantum measurement. The fraction of quantum measurements that survive to the end is $e^{-kt/\Lambda}$ because of k electron passing events. Hence we replace the number of quantum measurements N/k with $Ne^{-kt/\Lambda}/k$. We thus modify the above relation $kN \simeq \delta\theta^{-2}$ to $kNe^{-kt/\Lambda} \simeq \delta\theta^{-2}$. The optimal k that maximizes $\delta\theta^{-2}$ is $k_{opt} = \Lambda/t$, where we have a relation $\delta\theta \simeq \sqrt{e/k_{opt}N}$. Improvement over the shot noise limit $\delta\theta \simeq 1/\sqrt{N}$ in terms of the phase measurement precision is therefore $\sqrt{k_{opt}/e} = \sqrt{\Lambda/et} \simeq \sqrt{100 \text{ nm}/t}$. As we see below, this is not much of an improvement.

Specimens cannot be made arbitrarily thin. To begin with, t should not be smaller than the size of biological molecules, e.g. ~ 10 nm, unless we are able to slice the molecules without significantly damaging their structure at the plane of slicing. The state of the art in specimen thinning is as follows. In SPA, preparation of $30 \sim 50$ nm-thick specimens “remains quite unreliable”

[21], although “very reproducible average ice thickness of 15–20 nm” has also been reported recently [22]. The situation is different in ECT. In the method of cryo-electron microscopy of vitreous sections (CEMOVIS), the specimen thickness is “rarely less than 50 nm” [23]. Moreover, the thickness of the “damage layer” generated by gallium focused ion beam milling on the resultant specimen surface “could probably be kept to around 5 nm” [24]. A previous estimation of QEM performance, which considered inelastic scattering processes, assumed $t = 17.5$ nm [13]. The acceptable specimen thickness should obviously be greater for wide applicability of QEM possibly into ECT.

Our understanding of radiation damage in cryoEM is improving. Electron irradiation destroys biological specimens, starting from small structural features progressively towards larger ones. A recent study [19] on a purple membrane 2-dimensional crystal describes this behavior in a way that is particularly amenable to theoretical analysis. Let the scattering vector be $\mathbf{q} = \mathbf{k}_f - \mathbf{k}_i$, where $\mathbf{k}_i, \mathbf{k}_f$ are electron wave vectors before and after scattering and $q = |\mathbf{q}|$. The intensity of the electron wave scattered off the crystal at a diffraction plane is found to decay as $I = I_0 e^{-RFq^2/8\pi^2}$, where I is the intensity, I_0 is the initial intensity, $R \simeq 7 \times 10^{-4} \text{ nm}^4$ is a constant, F is electron fluence. The intensity I_0 is large at small q , while high-resolution signal at large q is weak [25]. Although the particular value of R above pertains to purple membrane with 300 keV imaging electrons, we assume that the value generalizes fairly well to other proteins. We call $B = RF$ the B -factor here although this represents radiation damage rather than thermal effect. Note that the relation $B = RF$ has a natural interpretation that electron irradiation basically causes random walks of atoms, recalling that the standard B -factor expresses thermal effects and hence the square of atomic displacements. More precisely, one can show that $\sqrt{B/8\pi^2}$ is the standard positional deviation of atoms from the original location, assuming that all atoms random walk in the same manner [26].

The initial period of the measurement is *crucial* in obtaining high resolution information. Let A be the area of electron beam illumination and $\sigma = \frac{2\pi}{q}$ be the resolution of interest. In the interpretation that $B/8\pi^2$ is essentially the mean squared distance traveled by random-walking atoms under electron irradiation, structural information on the length scale σ should be obtained before electron fluence F reaches $F_{opt} = \frac{8\pi^2\sigma^2}{R}$, where $\gamma = \mathcal{O}(1)$ is a numerical constant. An “optimal” value $\gamma = 0.064$ may be derived under certain assumptions [27]. The electron fluence that one can expend in a ring-shaped resolution band $[q, q + \Delta q]$ is $\Delta F = F_{opt}(q) - F_{opt}(q + \Delta q) \simeq -\frac{dF_{opt}(q)}{dq}\Delta q = -\frac{d}{dq}\left(\gamma\frac{32\pi^4}{Rq^2}\right)\Delta q = \gamma\frac{64\pi^4}{Rq^3}\Delta q$. There are $\frac{2\pi q}{\Delta q}$ square-shaped regions with the side length Δq in the band $[q, q + \Delta q]$ in the q -space. Measurements at two square regions at $\pm\mathbf{q}$ yield amplitude and phase information about the corresponding spatial frequency component. Thus, the fluence budget for the measurement at

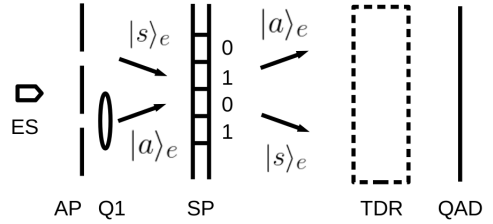


FIG. 1: An idealized QEM scheme for detecting the phase difference between two striped specimen regions 0 and 1. It comprises an electron source (ES), an aperture plate (AP), a ring-shaped qubit (Q1), a specimen (SP), a time-of-flight drift region (TDR) and a quantum area detector (QAD). A quantum computer (QC, not shown) is connected to Q1 and QAD. Lenses are not shown. The scheme is for conceptual discussions. Practical aspects should be dealt with in further study.

each square-shaped region is $F_{sq} = \frac{\Delta F}{2\pi q/\Delta q} = \gamma\frac{32\pi^3}{Rq^4}\Delta q^2$. Later we perform discrete Fourier transform when simulating our method, where Δq should represent the discretized step of angular spatial frequency and $A \cdot \Delta q^2 = (2\pi)^2$. Hence we obtain the corresponding electron dose $N_{sq} = F_{sq}A = \gamma\frac{8\pi\sigma^4}{R} = 2.3 \times 10^3 (\gamma/0.064) (\sigma/\text{nm})^4$, which does not depend on A . This quartic dependence highlights the importance of the initial period of the measurement and suggests measurement schemes that scan the reciprocal q -space, beginning at a large q region and progressively moving inwards.

Figure 1 illustrates a QEM scheme for acquiring data at a chosen spatial frequency \mathbf{q} . This turns out to be also effective in handling inelastic scattering. To make theoretical analysis simpler, it involves a quantum computer (QC) and time-of-flight (TOF) drift region (TDR). Let the generic notation of symmetric/asymmetric states be $|s\rangle = (|0\rangle + |1\rangle)/\sqrt{2}$ and $|a\rangle = (|0\rangle - |1\rangle)/\sqrt{2}$, respectively. We write a state of the composite system of an electron and the qubit Q1 as $|uv\rangle \equiv |u\rangle_e \otimes |v\rangle_q$. Let z be the optical axis and $\lambda = 2\pi/k_z$ be the electron wavelength. An electron emitted from the pulsed electron source ES goes through a stencil mask on a diffraction plane with two apertures AP with an equal amplitude. Let the quantum state of the electron wave going through each aperture be $|s\rangle_e$ and $|a\rangle_e$, respectively. Let the state of Q1 located near the aperture, where the state $|a\rangle_e$ is associated, be $|s\rangle_q + i\alpha|a\rangle_q$, where α is small. An electron passing through Q1 flips its state between $|s\rangle_q$ and $|a\rangle_q$ [14]. This results in an entangled state $(|ss\rangle + |aa\rangle) + i\alpha(|sa\rangle + |as\rangle)$. Upon electron transmission through the specimen, either inelastic electron scattering occurs or otherwise, which we can determine by TOF measurement. Either way, the scattered electron wave is captured by a quantum area detector (QAD) [14, 28] as a *quantum state*. To be specific, let the QAD be on an image plane. We may perform *any* operation on the captured state in the QC connected to the QAD and Q1.

First, consider a hypothetical case for simplicity, where no inelastic scattering occurs and the electron state remains in the space spanned by $|s\rangle_e$ and $|a\rangle_e$ after scattering. Unitarity only permits the form of scattering $|s\rangle_e \rightarrow |s\rangle_e + (i\varepsilon - \eta)|a\rangle_e$ and $|a\rangle_e \rightarrow |a\rangle_e + (i\varepsilon + \eta)|s\rangle_e$, where ε, η are small real parameters. The state of the entire system after scattering is $(|ss\rangle + |aa\rangle) + i(\alpha + \varepsilon)(|sa\rangle + |as\rangle) + \eta(|sa\rangle - |as\rangle)$. Measurement of the scattered electron state with respect to the basis $\{|s\rangle_e, |a\rangle_e\}$ results in a qubit state $|s\rangle_q + \{i(\alpha + \varepsilon) + \eta\}|a\rangle_q$ or $|a\rangle_q + \{i(\alpha + \varepsilon) - \eta\}|s\rangle_q$ depending on the measurement outcome, which is then used to conditionally manipulate the qubit to obtain the state $|s\rangle_q + \{i(\alpha + \varepsilon) \pm \eta\}|a\rangle_q$ by an operation $|s\rangle_q \leftrightarrow |a\rangle_q$. To obtain quantum advantage, we repeat this process k times after initially setting $\alpha = 0$, resulting in a state $\simeq |s\rangle_q + (ik\varepsilon \pm \sqrt{k}\eta)|a\rangle_q$, where \sqrt{k} comes from random walking. A unitary operation on the qubit yields amplitudes $(1 + k\varepsilon \mp i\sqrt{k}\eta)/\sqrt{2}$ and $(1 - k\varepsilon \pm i\sqrt{k}\eta)/\sqrt{2}$, which translate to probabilities $[(1 \pm k\varepsilon)^2 + k\eta^2]/2 \simeq 1/2 \pm k\varepsilon$. This is basically another view of the same process described in terms of the basis $\{|0\rangle_e, |1\rangle_e\}$ previously [11, 12]. In this latter view, we measure the phase difference between two interleaved, striped specimen regions illuminated by $|0\rangle_e$ and $|1\rangle_e$ (See Fig. 1).

In reality, the electron state leaks from the two-state Hilbert space mentioned above. Consider elastic electron scattering first. We do not know the two amplitudes of scattered waves respectively from the two incident waves $|s\rangle_e$ and $|a\rangle_e$ at a particular point on the diffraction plane where the electron is detected. Hence detection of an elastically scattered electron leads to an unknown qubit state, thereby destroying the measurement. We avoid this by “obscuring the fact” that elastic scattering ever happened, by recombining the scattered wave with the primary wave. Let the number of pixels of the QAD be M^2 and label each pixel with two integers n, m ranging from $-M/2$ to $M/2 - 1$, which respectively represents x and y coordinates. The procedure follows, while step-by-step calculations are described in Supplemental Material [29]. First, capture the exit electron wave by the QAD placed on an image plane. Appropriate setting of incident angles of the electron beam $|s\rangle_e$ and $|a\rangle_e$ allows us to obtain the state of the form $\sum_{n,m} (1 + i\theta_{n,m}) c_{n,m} |n, m\rangle_d$, where $|n, m\rangle_d$ is a QAD state and $c_{n,m}$ equals

$$e^{i\frac{\pi}{2}n} (|s\rangle_q + i\alpha|a\rangle_q) + e^{-i\frac{\pi}{2}n} (|a\rangle_q + i\alpha|s\rangle_q), \quad (1)$$

while $\theta_{n,m}$ represents the phase shift map of the specimen with zero mean. Second, perform quantum fast Fourier transform (qFFT) [30] on the QAD qubits, virtually obtaining the state on the diffraction plane. We obtain large amplitudes at the two states $|\pm M/4, 0\rangle_d$, which correspond to the two transmitted waves $|s\rangle_e$ and $|a\rangle_e$. Third, multiply i to the states $|\pm M/4, 0\rangle_d$, which may be viewed as a “virtual $\pi/2$ phase plate”. Fourth, set aside the qubit Q2 in the QAD that holds values 0

and 1 respectively for the states $n < 0$ and $n \geq 0$ of $|n, m\rangle_d$. Apply inverse qFFT (iqFFT) to all the other qubits, meaning that we apply iqFFT to the two half planes $n < 0$ and $n \geq 0$ separately. Let $\theta_{n,m}^L$ and $\theta_{n,m}^H$, where $-M/4 \leq n < M/4$, be respectively low-pass filtered, and high-pass filtered, versions of $\theta_{n,m}$. The cut-off frequency is sharply at $n = \pm M/4$ in the reciprocal space. Fifth, measure the QAD state with respect to the basis $\{|n, m\rangle_d\}$. Let the measurement results, *ignoring* the Q2 bit, be \hat{n}, \hat{m} . If Q2 indicates 0, the state of Q1 is

$$(1 - \alpha\bar{\theta} + \theta_{\hat{n}, \hat{m}}^L + i\alpha\theta_{\hat{n}, \hat{m}}^H) |s\rangle_q + i(\alpha + \bar{\theta} + \alpha\theta_{\hat{n}, \hat{m}}^L - i\theta_{\hat{n}, \hat{m}}^H) |a\rangle_q, \quad (2)$$

where $\bar{\theta} = (1/M^2) \sum_{n,m} (-1)^n \theta_{n,m}$ is the phase component of the specific spatial frequency that we wish to measure. If Q2 shows 1, the Q1 state equals the one obtained by applying the operation $|s\rangle_q \leftrightarrow |a\rangle_q$ to Eq. (2). We may expect that the product of the accumulated phase α and the various forms of phase shift $\theta_{\hat{n}, \hat{m}}^L, \theta_{\hat{n}, \hat{m}}^H, \bar{\theta}$ is small. When this is the case, Eq. (2) is simplified to $(1 + \theta_{\hat{n}, \hat{m}}^L) |s\rangle_q + i(\alpha + \bar{\theta} - i\theta_{\hat{n}, \hat{m}}^H) |a\rangle_q$. We see that both errors coming from $\theta_{\hat{n}, \hat{m}}^L$ and $\theta_{\hat{n}, \hat{m}}^H$, which vary randomly for each step of k repetitions, have small, second-order effect on the eventual measurement on Q1.

At first glance, getting errors from *elastic* scattering processes may seem odd. However, one can show that conventional in-focus phase contrast measurement suffers from a similar problem when we measure a small high-spatial frequency component superposed on a typically much greater low-spatial frequency component [31]. From the conceptual perspective, in our QEM scheme we protect, to a degree, high-resolution measurement from the influence of larger, low-resolution parts. In particular, we do not quantum-enhance the low-resolution signals. One might find this “protection” somewhat similar to cooling because we let “entropy” out by measuring quasi-random data (\hat{n}, \hat{m}) on the QAD.

Inelastic scattering poses a seemingly insurmountable problem. The reason is that deposition of energy at a particular point on the specimen would localize the electron to one of the two regions 0, 1 (Fig. 1), destroying the needed coherence. However, inelastic scattering is somewhat delocalized [32] and hence the problem is less severe at *higher* resolution. In the far field, the degree of localization manifests itself as the angular spread of the inelastically scattered wave. For example, if excitation of an atom caused localization of the electron wave to an atomic dimension δx , then the spread of the scattered wave $\sim \lambda/\delta x$ would be much larger than what is observed. In our scheme, the problem is to decide whether the detected electron originates from the incident state $|s\rangle_e$ or $|a\rangle_e$, in spite of the angular spread caused by inelastic scattering. Let the mass and velocity of the electron be m and v , respectively. The typical energy loss due to plasmons is $\Delta E \simeq 20$ eV [33].

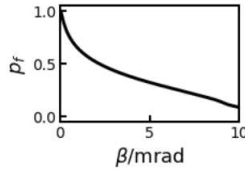


FIG. 2: Failure probability p_f to neutralize the effect of inelastic scattering as a function of the angle $\beta = \lambda/\sigma$, where σ represents the target resolution.

Bethe theory tells us that the scattering cross section is $\propto (\beta^2 + \beta_E^2)^{-1}$, where $\beta = q/k_z$ is the scattering angle and $\beta_E = \sqrt{1 - (v/c)^2 \Delta E/mv^2}$ [32].

For simplicity, we make several assumptions. First, energy loss ΔE is always 20 eV. (In principle, one could measure ΔE and perform the best possible operation that depends on the value of ΔE .) Second, we ignore small wavefront distortion due to simultaneous elastic scattering. Third, no scattering is assumed to occur above the cutoff angle $\beta_c = \sqrt{2\beta_E}$ at the Bethe-ridge. Fourth, we assume zero phase variation of the exit electron wave, although better modeling is certainly desirable [34]. Thus the Hankel-transformed far-field wave amplitude $(\beta^2 + \beta_E^2)^{-1/2}$ also have zero phase variation. Finally, electrons get entangled with the specimen upon inelastic scattering [35], resulting in a mixed quantum state. We ignore this effect. However, preliminary remarks are presented in Supplemental Material [36].

Under the simplifying assumptions mentioned above, our task boils down to distinguishing the two inelastically scattered electron states $|s'\rangle_e, |a'\rangle_e$ captured by the QAD. Their form on the diffraction plane is $(\beta^2 + \beta_E^2)^{-1/2}$ with the cutoff β_c , where the central point ($\beta = 0$) matches respectively to those of the incident waves $|s\rangle_e$ and $|a\rangle_e$. Perfect discrimination of $|s'\rangle_e, |a'\rangle_e$ is impossible because of the overlap between them. To achieve the best possible, we use the Ivanovic-Dieks-Peres (IDP) scheme [37–39], in which the failure probability is $p_f = |\langle s'|a'\rangle_e|$. We have full confidence when an IDP measurement succeeds, or we have zero information and the measurement fails completely. Numerically computed p_f , as a function of β , which in this case is the angle between the incident waves $|s\rangle_e$ and $|a\rangle_e$, is shown in Fig. 2 [40]. The angular spread of incident electron beams $|s\rangle_e$ and $|a\rangle_e$ is assumed to be below $\beta_E = 41 \mu\text{rad}$ [40]. The probability of inelastic scattering is reduced, in effect, by a factor p_f , which is especially effective at high resolutions.

To visually assess the improvement afforded by the scheme, we simulate imaging of the Marburg virus VP35 domain molecule [41]. Figure 3 shows the result. The electron phase (shift) map is computed as described in Supplemental Material [42]. The parameter value $\gamma = 0.064$ [27] is used to obtain the images. The simulated images are addition of the phase map and noise, which are then filtered for visibility. The improvement by inelastic

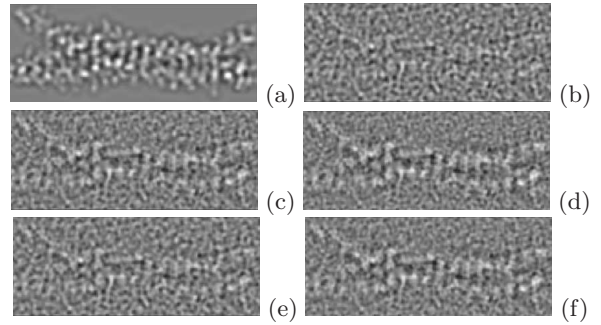


FIG. 3: Simulated images of the Marburg virus VP35 domain molecule [41]. (a) A band-pass filtered phase map. (b) Imaging without quantum enhancement, i.e. the repetition number $k = 1$. (c) QEM imaging without inelastic scattering neutralization (ISN), wherein $k = 10$, roughly corresponding to a specimen thickness $t \simeq 30 \text{ nm}$. (d) QEM imaging with ISN. The repetition number is essentially k/p_f , where $k = 10$. (e) QEM imaging without ISN, wherein $k = 5$ (i.e. specimen thickness $t \simeq 60 \text{ nm}$). (f) QEM imaging with ISN, wherein $k = 5$. The horizontal length of all images is 10 nm.

scattering neutralization (ISN) is mainly at high resolution and visually rather subtle, requiring removal of large low resolution components. Thus all six images are filtered by multiplying a function $e^{-\beta^2/2\beta_H^2} (1 - e^{-\beta^2/2\beta_L^2})$ in the q space, where $\beta_L = 2 \text{ mrad}$ and $\beta_H = 3.5 \text{ mrad}$. Figure 3 (a) shows the zero-noise case. The noise component is generated as follows [43]. First, gaussian random number with zero mean and unit variance is supplied to each pixel in the image plane. Second, we Fourier transform it to get a complex-valued distribution on the diffraction plane. We then multiply a function $\Delta\theta(\beta)$ representing phase noise spectrum (PNS) under consideration. Finally, we use inverse Fourier transform to get real-space noise. Figure 3 (b) shows the “classical” case $\Delta\theta_c(\beta) = 1/\sqrt{N_{sq}}$, where N_{sq} is expressed as a function of β . Figure 3 (c) shows the case for QEM with fixed $k = 10$, where $\Delta\theta_{q1}(\beta) = \sqrt{e/k_1} \Delta\theta_c(\beta)$ and $k_1 = \min(k, N_{sq})$. The “min” function, which returns the smallest value, ensures that the repetition number does not exceed N_{sq} . Figure 3 (d) shows the case for QEM with ISN. The PNS in this case is $\Delta\theta_{q2}(\beta) = \sqrt{p_f(\beta) e/k_2} \Delta\theta_c(\beta)$, where p_f is the aforementioned failure probability and $k_2 = \min(k/p_f(\beta), N_{sq})$. Alternatively, using ISN one can essentially maintain the image quality shown in Fig. 3 (c) while increasing the specimen thickness by a factor $1/p_f \simeq 2$ at $\beta_L < \beta < \beta_H$. Figure 3 (e) shows the case $k = 5$, which means the specimen thickness is roughly $t = \Lambda/k \simeq 60 \text{ nm}$, without ISN. Figure 3 (f) show the same $k = 5$ case with ISN. All the difference between Figs. (c)-(d) and Figs. 3 (e)-(f), respectively, is the k value employed in computation.

The author thanks Professor Ray F. Egerton for useful discussions. This research was supported in part by the JSPS “Kakenhi” Grant (Grant No. 19K05285).

[1] R. Henderson, The potential and limitations of neutrons, electrons and X-rays for atomic resolution microscopy of unstained biological molecules, *Quart. Rev. Biophys.* **28**, 171-193 (1995).

[2] T. Grant and N. Grigorieff, Measuring the optimal exposure for single particle cryo-EM using a 2.6 reconstruction of rotavirus VP6, *eLife* **4**, e06980 (2015).

[3] R. M. Glaeser, Cryo-electron microscopy of biological nanostructures, *Phys. Today*, **61**, 48-54 (2008).

[4] W. P. Putnam and M. F. Yanik, Noninvasive electron microscopy with interaction-free quantum measurements, *Phys. Rev. A* **80**, 040902 (2009).

[5] S. Thomas, C. Kohstall, P. Kruit, and P. Hommelhoff, Semitransparency in interaction-free measurements, *Phys. Rev. A* **90**, 053840 (2014).

[6] P. Kruit, R. G. Hobbs, C-S. Kim, Y. Yang, V. R. Manfrinato, J. Hammer, S. Thomas, P. Weber, B. Klopfer, C. Kohstall, T. Juffmann, M. A. Kasevich, P. Hommelhoff, and K. K. Berggren, Designs for a quantum electron microscope, *Ultramicroscopy* **164**, 31-45 (2016).

[7] T. Juffmann, S. A. Koppell, B. B. Klopfer, C. Ophus, R. M. Glaeser, and M. A. Kasevich, Multi-pass transmission electron microscopy, *Sci. Rep.* **7**, 1699 (2017).

[8] A. Agarwal, K. K. Berggren, Y. J. van Staaden, and V. K. Goyal, Reduced damage in electron microscopy by using interaction-free measurement and conditional reillumination, *Phys. Rev. A* **99**, 063809 (2019).

[9] M. Turchetti, C-S. Kim, R. Hobbs, Y. Yang, P. Kruit, and K. K. Berggren, Design and simulation of a linear electron cavity for quantum electron microscopy, *Ultramicroscopy* **199**, 50-61 (2019).

[10] S. A. Koppell, M. Mankos, A. J. Bowman, Y. Israel, T. Juffmann, B. B. Klopfer, and M. A. Kasevich, Design for a 10 keV multi-pass transmission electron microscope, *Ultramicroscopy* **207**, 112834 (2019).

[11] H. Okamoto, Possible use of a Cooper-pair box for low-dose electron microscopy, *Phys. Rev. A* **85**, 043810 (2012).

[12] H. Okamoto and Y. Nagatani, Entanglement-assisted electron microscopy based on a flux qubit, *Appl. Phys. Lett.* **104**, 062604 (2014).

[13] H. Okamoto, Measurement errors in entanglement-assisted electron microscopy, *Phys. Rev. A* **89**, 063828 (2014).

[14] H. Okamoto, Quantum interface to charged particles in a vacuum, *Phys. Rev. A* **92**, 053805 (2015).

[15] R. Englmeier and F. Frster, Cryo-electron tomography for the structural study of mitochondrial translation, *Tissue Cell*, **57**, 129-138 (2019).

[16] W. Baumeister, Mapping molecular landscapes inside cells, *Biol. Chem.* **385**, 865-872 (2004).

[17] P. B. Rosenthal and R. Henderson, Optimal determination of particle orientation, absolute hand, and contrast loss in single-particle electron cryomicroscopy, *J. Mol. Biol.* **333**, 721-745 (2003).

[18] H. Dou, D. W. Burrows, M. L. Baker, and T. Ju, Flexible fitting of atomic models into cryo-EM density maps guided by helix correspondences, *Biophys. J.* **112**, 2479-2493 (2017).

[19] M. J. Peet, R. Henderson, and C. J. Russo, The energy dependence of contrast and damage in electron cryomi-
croscopy of biological molecules, *Ultramicroscopy* **203**, 125-131 (2019).

[20] M. Vulovic, R. B. Ravelli, L. J. van Vliet, A. J. Koster, I. Lazic, U. Lucken, H. Rullgard, O. Oktem, and B. Rieger, Image formation modeling in cryo-electron microscopy, *J. Struct. Biol.* **183**, 19-32 (2013).

[21] R. M. Glaeser, B.-G. Han, R. Csencsits, A. Killilea, A. Pulk, and J. H. D. Cate, Factors that influence the formation and stability of thin, cryo-EM specimens, *Biophys. J.* **110**, 749-755 (2016).

[22] W. J. Rice, A. Cheng, A. J. Noble, E. T. Eng, L. Y. Kim, B. Carragher, and C. S. Potter, Routine determination of ice thickness for cryo-EM grids, *J. Struct. Biol.* **204**, 38-44 (2018).

[23] B. Zuber, M. Chami, C. Houssin, J. Dubochet, G. Griffiths, and M. Daffe, Cryo-electron microscopy of vitreous sections. In: Aretz A., Hermanns-Sachweh B., Mayer J. (eds) *EMC 2008 14th European Microscopy Congress 1–5 September 2008, Aachen, Germany*. Springer, Berlin, Heidelberg (2008).

[24] M. Marko, C. Hsieh, W. Moberlychan, C. A. Mannella, and J. Frank, Focused ion beam milling of vitreous water: prospects for an alternative to cryo-ultramicrotomy of frozen-hydrated biological specimens, *J. Microsc.*, **222**, 42–47 (2006).

[25] See Supplemental Material I.

[26] See Supplemental Material II.

[27] See Supplemental Material III.

[28] See Supplemental Material IV.

[29] See Supplemental Material V.

[30] D. R. Simon, On the power of quantum computation, *SIAM J. Comput.*, **26**, 1474-1483 (1997).

[31] See Supplemental Material VI.

[32] R. F. Egerton, *Electron Energy-Loss Spectroscopy in the Electron Microscope*, 3rd edition (Springer, Berlin, 2011).

[33] R. Leapman and S. Sun, Cryo-electron energy loss spectroscopy: observations on vitrified hydrated specimens and radiation damage, *Ultramicroscopy* **59**, 71-19 (1995).

[34] R. F. Egerton, Calculation, consequences and measurement of the point spread function for low-loss inelastic scattering, *Microscopy*, **67**, i52–i59 (2018).

[35] P. Schattschneider and S. Loeffler, Entanglement and decoherence in electron microscopy, *Ultramicroscopy* **190**, 39-44 (2018).

[36] See Supplemental Material VII.

[37] I. D. Ivanovic, How to differentiate between non-orthogonal states, *Phys. Lett. A* **123**, 257-259 (1987).

[38] D. Dieks, Overlap and distinguishability of quantum states, *Phys. Lett. A* **126**, 303-306 (1988).

[39] A. Peres, How to differentiate between non-orthogonal states, *Phys. Lett. A* **128**, 19 (1988).

[40] See Supplemental Material XIII.

[41] J. F. Bruhn, R. N. Kirchdoerfer, S. M. Urata, S. Li, I. J. Tickle, G. Bricogne, and E. Ollmann Saphire, Crystal structure of the Marburg virus VP35 oligomerization domain, *J. Virol.* **91**, e01085-16 (2017).

[42] See Supplemental Material IX.

[43] See Supplemental Material X.

Supplemental Material for “Resilient Quantum Electron Microscopy”

In the followings, some symbols denote multiple quantities to avoid cluttered presentation. For example, the symbol σ denotes resolution in the main text, scattering cross section in Sec. I, and standard deviation in Sec. X. However, the intention should be clear from the context.

I. STRUCTURAL FEATURES OF BIOLOGICAL MOLECULES

To evaluate the performance of QEM, it is useful to know some general facts about cryoEM specimens. In this section, we focus on elastic scattering from a molecule. Consider a hypothetical diffraction intensity pattern I_0 free from the effect of radiation damage. The intensity I_0 is proportional to the scattering cross section $\frac{d\sigma}{d\Omega}$

$$I_0 \propto \frac{d\sigma}{d\Omega} = \left| \sum_s f_s(\theta) e^{-i\mathbf{q} \cdot \mathbf{r}_s} \right|^2, \quad (\text{S1})$$

where $f_s(\theta)$ is the electron scattering amplitude of the s -th atom with the scattering angle θ , \mathbf{r}_s is the position of the s -th atom, and $\mathbf{q} = \mathbf{k}_f - \mathbf{k}_i$ is the change of the wave vector of the electron upon scattering (the scattering vector). The function $f_s(\theta)$ has angular spread of $\simeq 10$ mrad for 300 keV electrons and $f(0) \simeq (0.3 \sim 0.4)$ nm for relevant elements except the hydrogen. We focus, for the moment, on features larger than 0.2 nm = $\lambda/(10$ mrad), where $\lambda = 1.97$ pm is the wavelength of 300 keV electrons, and hence we replace $f_s(\theta)$ with $f_s \equiv f_s(0)$. Moreover, we ignore the small imaginary part of $f_s(0)$. The scattering cross section is then expressed as

$$\frac{d\sigma}{d\Omega} = \left| \int d\mathbf{r} \rho(\mathbf{r}) e^{-i\mathbf{q} \cdot \mathbf{r}} \right|^2, \quad (\text{S2})$$

where $\rho(\mathbf{r})$ is the “density of scattering amplitude” per unit volume. This is also expressed as $\frac{d\sigma}{d\Omega} = |\eta(\mathbf{q})|^2$, where $\eta(\mathbf{q}) = \int d\mathbf{r} \rho(\mathbf{r}) e^{-i\mathbf{q} \cdot \mathbf{r}}$ has the property $\eta(-\mathbf{q}) = \eta^*(\mathbf{q})$ because $\rho(\mathbf{r}) \in \mathbb{R}$.

Biological molecules share some common structural features [S1]. We divide I_0 roughly into two regions. First, at small q we have an expectation value, on averaging over the molecule’s orientations,

$$\frac{d\sigma}{d\Omega} \simeq \Sigma_0 e^{-R_g^2 q^2/3} \quad (\text{S3})$$

as usually found in the Guinier plot, where $\Sigma_0 = \{\eta(0)\}^2 = \{\sum_s f_s\}^2$ and R_g is the radius of gyration of the molecule under study. Data in this region represent the overall shape of the molecule. In the remaining second region with large q , the scattered waves from the atoms in the specimen interfere in essentially a random manner. This is where the high resolution structural data are. We model the molecule as a set of randomly placed atoms, i.e. $\rho(\mathbf{r}) = \sum_s f_s \delta(\mathbf{r} - \mathbf{r}_s)$. This results in, on average,

$$\frac{d\sigma}{d\Omega} = \sum_s f_s^2 + \sum_{s \neq l} f_s f_l \cos[\mathbf{q} \cdot (\mathbf{r}_s - \mathbf{r}_l)] \simeq \sum_s f_s^2. \quad (\text{S4})$$

The last approximation is valid when q is sufficiently large and the cosine factor essentially gives a random sign. (The *magnitude* of the second term is as large as that of the first term.)

Typical biological molecules are weak phase objects. Let the specimen be on the xy -plane and let the electron optical axis be z -axis. We project a vector \mathbf{r} onto the xy -plane to get a 2-dimensional (2D) vector $\hat{\mathbf{r}}$. Let $\gamma(\hat{\mathbf{r}})$, defined on the xy -plane, be the projected density of scattering amplitude $\rho(\mathbf{r})$ onto the xy -plane, i.e. $\gamma(\hat{\mathbf{r}}) = \int dz \rho(\mathbf{r})$. Its 2D Fourier transform $\int d\hat{\mathbf{r}} \gamma(\hat{\mathbf{r}}) e^{-i\hat{\mathbf{q}} \cdot \hat{\mathbf{r}}}$ equals $\eta(\hat{\mathbf{q}})$, where the 2-dimensional vector $\hat{\mathbf{q}}$ is to \mathbf{q} as $\hat{\mathbf{r}}$ is to \mathbf{r} . Under the projection assumption, the phase shift θ induced on the passing electron wave is given as $\theta(\hat{\mathbf{r}}) = \lambda \gamma(\hat{\mathbf{r}})$ [S2]. The above relation $\frac{d\sigma}{d\Omega} \simeq \sum_s f_s^2$ implies

$$|\eta(\hat{\mathbf{q}})| \simeq \sqrt{\sum_s f_s^2}, \quad (\text{S5})$$

which roughly is proportional to the square root of the number of atoms N comprising the molecule illuminated by the electron beam. We consider a molecule of an areal size \hat{A} and ignore the surrounding water molecules. This

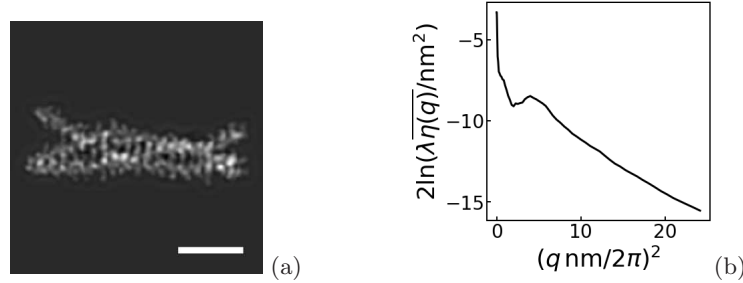


FIG. S1: (a) A phase map of the Marburg virus VP35 domain molecule (5TOI). Scale bar: 3 nm. (b) The Guinier plot of the molecule 5TOI. We see a broad peak with the corresponding length ~ 0.5 nm and an approximately linear slope corresponding to a B -factor of 0.7 nm^2 at higher spatial frequencies.

simplification is arguably justified because water molecules are known to move during electron exposure [S3]. The power spectral density $S(\hat{\mathbf{q}})$ associated with $\theta(\hat{\mathbf{r}})$ is

$$S(\hat{\mathbf{q}}) = \frac{1}{\hat{A}} \left| \int \theta(\hat{\mathbf{r}}) e^{-i\hat{\mathbf{q}} \cdot \hat{\mathbf{r}}} d\hat{\mathbf{r}} \right|^2 = \lambda^2 \frac{|\eta(\hat{\mathbf{q}})|^2}{\hat{A}} \simeq \lambda^2 \frac{\sum_s f_s^2}{\hat{A}} = n \lambda^2 f^2, \quad (\text{S6})$$

where $n = N/\hat{A}$ is the areal number density of relevant atoms and f represents the root mean square of the set $\{f_s | s \in \mathbb{N}\}$.

The above overall picture is consistent with the following empirical data. Figure S1(a) shows a simulated in-focus phase contrast cryoEM image (See Sec. IX) of a hypothetical radiation-resistant Marburg virus VP35 oligomerization domain (Protein Data Bank (PDB) ID: 5TOI), where atomic coordinates are obtained by X-ray crystallography [S5]. This is a protein molecule with 25 kDa molecular weight, which may be regarded as “average” [S6], comprising $\simeq 3.3 \times 10^3$ atoms. Taking the rough areal size of the molecule as $\hat{A} = 23 \text{ nm}^2$ (See Sec. IX), we obtain

$$S(\hat{\mathbf{q}}) \simeq \lambda^2 \frac{\sum_s f_s^2}{\hat{A}} \simeq (6.4 \text{ pm})^2 = (6.4 \text{ mrad} \cdot \text{nm})^2 \quad (\text{S7})$$

from the above argument based on randomly placed atoms. The scattering amplitude data for computing Eq. (S7) is obtained from Ref. [S4]. All atoms are counted except hydrogen atoms, for which the method described in the last paragraph of Sec. IX is used. On the other hand, Fig. S1 (b), i. e. the Guinier plot of the Marburg virus VP35 domain molecule (5TOI) [S5], shows the power spectrum pertaining to radially averaged $\eta(\mathbf{q})$. We found the Guinier plot remarkably similar to those of bacteriorhodopsin (1FBB) [S7] and aldolase (6ALD) [S8]. Let $\overline{\eta(\mathbf{q})}$ be the average value of $\eta(\mathbf{q})$ where $|\mathbf{q}| = q$ is satisfied upon taking the average. Beyond the broad peak at $q/2\pi = \sqrt{5} \text{ nm}^{-1}$ corresponding to the α -helix, we see a line representing a “ B -factor”, which satisfies $\overline{\eta(\mathbf{q})}^2 \propto e^{-\frac{B}{2}(\frac{q}{2\pi})^2}$, of about 0.7 nm^2 . This is much smaller than reported experimental values of $\sim 10 \text{ nm}^2$, which is understandable because radiation damage among other factors is involved in actual experiments [S1]. Instead, the “ B -factor” here is consistent with gaussian averaging (with $\sigma = 0.1 \text{ nm}$) involved in producing the inner potential map (See Sec. IX). The line representing the factor $e^{-\frac{B}{2}(\frac{q}{2\pi})^2}$ intersects the vertical axis at $\lambda \overline{\eta(\mathbf{q})} \simeq 0.03 \text{ nm}^2$, which gives a value of $S(\hat{\mathbf{q}}) = (\lambda \overline{\eta(\hat{\mathbf{q}})})^2 / \hat{A}$ that is consistent with the value mentioned above, i.e. $\simeq (6.4 \text{ mrad} \cdot \text{nm})^2$.

Finally, we estimate the magnitude of typical repetition number k . We are after a signal characterized by the power spectral density $S(\hat{\mathbf{q}}) \simeq n \lambda^2 f^2$, ignoring the “ B -factor”. The order of magnitude of its value is $\sim (10 \text{ mrad} \cdot \text{nm})^2$ for a typical specimen. Roughly speaking, one needs to detect phase shift $\theta \sim 10 \text{ mrad}$ to see a feature with size $\sim 1 \text{ nm}$ (or more precisely, to obtain information within a squared spatial angular frequency bandwidth $\sim (2\pi)^2 \times 1 \text{ nm}^{-2}$). If our main purpose is detection of the existence of such a phase shift θ , as opposed to quantification of it, then we may assert that $\theta = \delta\theta$. While it would take $N \simeq \theta^{-2} \simeq 10^4$ electrons to detect θ when limited by shot noise, we would only need $N \simeq \theta^{-1} \simeq 10^2$ electrons if Heisenberg limit were reached. QEM would operate somewhere in between these cases. For example, if we ignore inelastic scattering $k = 10$ gives $N \simeq \theta^{-2}/k \simeq 10^3$. Hence $k \simeq 10$ is the order of magnitude that we should consider, since it corresponds to the typical electron fluence $(1 \sim 2) \times 10^3 \text{ nm}^{-2}$.

II. “B-FACTOR” FOR DESCRIBING RADIATION DAMAGE

As in Sec. I, let the position and the electron scattering amplitude (having the dimension of length) of s -th atom be \mathbf{r}_s and f_s , respectively. The following argument is valid to the extent that f_s can be regarded as a constant within the range of scattering angle of interest. The scattering vector \mathbf{q} lies almost exactly in a plane perpendicular to the optical axis and hence $\mathbf{q} \simeq \hat{\mathbf{q}}$. The scattered electron wavefunction amplitude $\psi(\hat{\mathbf{q}})$ in the far field is proportional to

$$\psi(\hat{\mathbf{q}}) \propto \sum_s f_s e^{-i\hat{\mathbf{q}} \cdot \hat{\mathbf{r}}_s} = \int d^2 \hat{\mathbf{r}} \gamma(\hat{\mathbf{r}}) e^{-i\hat{\mathbf{q}} \cdot \hat{\mathbf{r}}}. \quad (\text{S8})$$

Since we suppose that atoms random walk, we should have the projected density of scattering amplitude $\gamma(\hat{\mathbf{r}})$ convoluted with

$$g(\hat{\mathbf{r}}) = \frac{1}{2\pi d^2} e^{-\frac{x^2+y^2}{2d^2}} \quad (\text{S9})$$

upon irradiation, where d is the standard positional displacement from the initial positions of atoms. Fourier transforming, we obtain the scattering amplitude that is $\psi(\hat{\mathbf{q}})$ multiplied by $\mathcal{F}\{g(\hat{\mathbf{r}})\} = e^{-\frac{d^2 q^2}{2}}$. Hence the initial intensity $I_0 = |\psi(\hat{\mathbf{q}})|^2$ at zero radiation damage is multiplied by $e^{-d^2 q^2}$. This allows us to identify d^2 with $B/8\pi^2$.

In the above reasoning, we implicitly assumed that there are *many* atoms random-walking so that $\gamma(\hat{\mathbf{r}})$ may be considered to be convoluted with a gaussian function. We note a limitation of this approach. After a long time, all the intensity on the diffraction plane is concentrated at $\hat{\mathbf{q}} = 0$ according to this model. In reality, all the atoms should still be there, having some particular positions rather than having smoothed out by gaussian averaging. Hence there should remain more or less random diffraction intensity in the far field. Monotonic decay of diffraction peaks in experiments on crystals [S9] results because changes due to radiation damage vary from molecule to molecule in the crystal.

III. ESTIMATION OF THE OPTIMAL γ VALUE

Here we describe how the value $\gamma = 0.064$ mentioned in the main text, which appears in the expression of F_{opt} , was obtained. Physically, too small a fluence F gives no statistical confidence, while too large an F yields data that mostly reflect altered structures due to radiation damage. Hence an optimal F_{opt} should exist.

In this attempt to find a useful γ value, we make a pragmatic assumption that a Fourier component $\theta_{\mathbf{q}}$ of the real-space map of weak phase shift $\theta(\mathbf{r})$ of the specimen decays to zero as $\theta_{\mathbf{q}}(F) = \theta_0 e^{-F/F_0}$ for some F_0 . Strictly speaking, this assumption cannot be entirely right (see the last paragraph of Sec. II) but we hope to obtain a useful estimate nonetheless. In the diffraction mode, as in the measurement in the quantitative study of radiation damage [S9], $\theta_{\mathbf{q}}^2$ is proportional to the diffraction intensity $I(\mathbf{q})$ and $\theta_{\mathbf{q}}(F) \propto e^{-RFq^2/16\pi^2}$. It follows that $F_0 = \frac{16\pi^2}{Rq^2} = \frac{4\sigma^2}{R} \simeq 6 \times 10^3 \text{ nm}^{-2} \cdot (\sigma/\text{nm})^2$. This allows us to ignore the specimen change during each quantum measurement with the repetition number $k \simeq \Lambda/t \simeq 10$ unless we are after very high resolution data. It can be shown that all relevant measurements in QEM boil down to measuring the parameter $k\theta$, given a quantum state $(|0\rangle + e^{ik\theta}|1\rangle)/\sqrt{2}$ (See Sec. XI). By expressing the state with measurement basis states $|\pm\rangle = (|0\rangle \pm i|1\rangle)/\sqrt{2}$, we obtain the corresponding probabilities $p_{\pm} = (1 \pm \sin k\theta)/2 \simeq (1 \pm k\theta_{\mathbf{q}}(F))/2$, where the last approximation requires $k\theta \ll 1$. Let X be a random variable that represents the number of events “+” occurring after $N_g = AF/k$ quantum enhanced measurements, each using a group of k electrons. The expectation value \bar{X} is given by

$$\bar{X} = \int p_+(N_g) dN_g \simeq \frac{N_g}{2} + \frac{k\theta_0}{2} \int_0^{N_g} e^{-kN_g'/AF_0} dN_g' = \frac{N_g}{2} + \frac{AF_0\theta_0}{2} \left(1 - e^{-kN_g/AF_0}\right), \quad (\text{S10})$$

while the variance is approximately a constant with respect to θ_0 , i.e.

$$\text{Var}(X) = \int p_+(N_g) p_-(N_g) dN_g \simeq \frac{N_g}{4}. \quad (\text{S11})$$

The estimator for θ_0 is

$$\hat{\theta}_0(X) = \frac{\beta/k}{1 - e^{-\beta}} \left(\frac{2X}{N_g} - 1 \right), \quad (\text{S12})$$

where $\beta = kN_g/AF_0 = F/F_0$. We obtain

$$\text{Var}(\hat{\theta}_0(X)) \simeq \frac{1}{kAF_0} \frac{\beta}{(1 - e^{-\beta})^2}, \quad (\text{S13})$$

which is minimized at $\beta_{opt} \simeq 1.26$, where $e^\beta = 2\beta + 1$ is satisfied. Hence we obtain $\gamma = F_{opt}/(2\pi^2 F_0) = \beta_{opt}/2\pi^2 \simeq 0.064$.

IV. REMARKS ON THE QUANTUM AREA DETECTOR

A design of the quantum area detector (QAD), which is able to capture the vacuum electron wave without ‘‘collapsing’’ the quantum state, has been described before [S10]. The purpose of this section is to point out that, in principle, the number of qubit can be reduced to a logarithm of the number of pixels. This could make QEM an excellent application of small-scale QC.

Figure S2 (a) shows the overall scheme, which is similar to the proposed obstruction-free phase plate scheme [S11, S12]. Let z -axis be the optical axis. For simplicity, we pretend that rotation of the electron beam around the optical axis due to a magnetic field etc. does not exist. We employ a device, similar to an aberration corrector, which elongates the electron beam in the direction of x -axis at one point on z -axis and then elongates the beam along y -axis at another point on z -axis, which is electron optically conjugate to the first point. At each of these two points, the elongated electron beam goes through a slit where qubits are placed. The position of the flying electron along the long direction of the slit, which is either x -axis or y -axis, is measured.

Consider a 4×4 pixel QAD. Figure S2 (b) shows a placement of 2 qubits, A and B, in the slit-shaped device that measures the x -coordinate of a flying electron. In the example shown, the electron flies ‘‘through’’ both the qubits and they are both excited from the initial state $|s\rangle$ to $|a\rangle$, resulting in the state $|a\rangle_A|a\rangle_B \equiv |aa\rangle_x$. (The ‘‘canonical form’’ of flux-based qubits, which operates as quantum interface to charged particles, includes a ring of magnetic flux, through which a charged particle passes [S10]. Feasible ways to realize such a qubit are currently under investigation. See Ref. [S13] for the most recent attempt.) In general, let the initial state of the electron be

$$|\psi\rangle_e = \sum_{x=0}^3 \sum_{y=0}^3 c_{x,y} |x, y\rangle_e, \quad (\text{S14})$$

where x, y are respectively the x and y -coordinate of the flying electron. By the principle of superposition, after passing the x -coordinate measurement device we obtain

$$|\Psi\rangle = \sum_{y=0}^3 \{c_{0,y}|0, y\rangle_e|ss\rangle_x + c_{1,y}|1, y\rangle_e|sa\rangle_x + c_{2,y}|2, y\rangle_e|as\rangle_x + c_{3,y}|3, y\rangle_e|aa\rangle_x\}. \quad (\text{S15})$$

Likewise, after passing the y -coordinate measurement device we obtain

$$|\Psi\rangle = c_{0,0}|0, 0\rangle_e|ss\rangle_x|ss\rangle_y + \dots + c_{3,3}|3, 3\rangle_e|aa\rangle_x|aa\rangle_y. \quad (\text{S16})$$

This is followed by classical detection of the electron in the far field, which multiplies certain phase factors onto each of the 16 QAD states. However, one can compensate for these phase factors in the manner described before (See Ref.[S10]. Also see the next paragraph for a 2-pixel case). Clearly, the foregoing argument may be generalized to the case of a $2^n \times 2^n$ pixel QAD comprising $2n$ qubits.

The size of QAD pixels should be sufficiently small. For simplicity, consider an *effective*, demagnified QAD on the specimen plane. The side length of the square-shaped pixel, l , should satisfy $l < \lambda/\theta$, where θ is about the largest angle between the optical axis and the electron trajectory. This results in minimal phase variation within the pixel. Otherwise we get errors due to high spatial frequency components of the wave function. To see this, consider two pixels placed side by side for simplicity, which constitute a single-qubit QAD. We indeed consider a 1-dimensional system because it suffices. Let pixel 0 occupy the range $-l < x < 0$ while pixel 1 occupies $0 < x < l$. Following the main text, let the QAD be on an image plane. Moreover, let the specimen be a phase object, albeit not necessarily a weak one. Let the two electron wave functions going through the two pixels be

$$\psi_0(x) = {}_e\langle x|0\rangle_e = \begin{cases} e^{i\theta(x)} & -l < x < 0 \\ 0 & \text{otherwise} \end{cases} \quad (\text{S17})$$

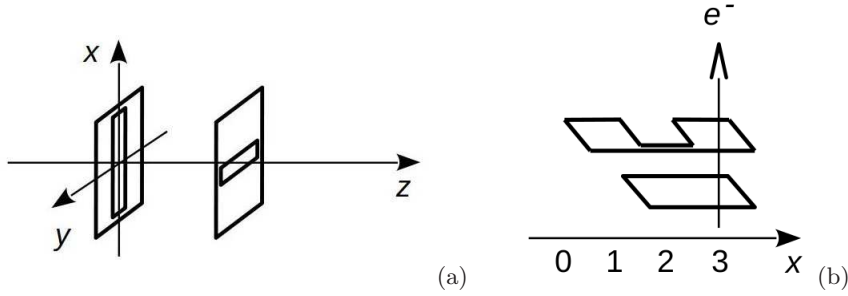


FIG. S2: Quantum area detector (QAD). (a) A QAD comprises two slits. Qubits are placed along the long direction of each slit. A classical electron area detector in the far field, placed on the far right, is not shown. The slit on the left measures the x -coordinate of the electron passing through the slit, while the one on the right likewise measures the y -coordinate. (b) Structure of the x -coordinate-measuring slit. Two qubits shown have a ring shaped magnetic flux (solid line segments) and detect an electron passing through the ring. Qubit A at the bottom measures the most significant bit (MSB) of the x -coordinate, while qubit B on top similarly measures the least significant bit (LSB).

and

$$\psi_1(x) = {}_e\langle x|1\rangle_e = \begin{cases} e^{i\theta(x)} & 0 < x < l \\ 0 & \text{otherwise} \end{cases}. \quad (\text{S18})$$

The entire system including the QAD-qubit is in a state

$$|0\rangle_e|\alpha\rangle_q + |1\rangle_e|\beta\rangle_q \quad (\text{S19})$$

for some $|\alpha\rangle_q$ and $|\beta\rangle_q$. Classical detection of the electron in the far field, i.e. in the state $\psi_k(x) = {}_e\langle x|k\rangle_e = e^{ikx}$, results in the qubit state

$${}_e\langle k|0\rangle_e|\alpha\rangle_q + {}_e\langle k|1\rangle_e|\beta\rangle_q = \frac{1}{l} \int_{-l}^0 e^{i[\theta(x)-kx]} dx |\alpha\rangle_q + \frac{1}{l} \int_0^l e^{i[\theta(x)-kx]} dx |\beta\rangle_q. \quad (\text{S20})$$

If the specimen is a weak phase object satisfying $\theta(x) \ll 1$ and the angle of deflection prior to the classical detection is small, i.e. $k \ll 2\pi/l$, then it is justifiable to expand the integrand as $e^{i[\theta(x)-kx]} \simeq 1 + i[\theta(x) - kx]$. Hence Eq. (S20) approximately equals

$$\simeq \left\{ 1 + i \left[\frac{1}{l} \int_{-l}^0 \theta(x) dx + k \left(\frac{l}{2} \right) \right] \right\} |\alpha\rangle_q + \left\{ 1 + i \left[\frac{1}{l} \int_0^l \theta(x) dx - k \left(\frac{l}{2} \right) \right] \right\} |\beta\rangle_q. \quad (\text{S21})$$

We know k because we measure it upon classical electron detection. Hence we can manipulate the QAD-qubit to obtain

$$\left\{ 1 + i \int_{-l}^0 \theta(x) dx \right\} |\alpha\rangle_q + \left\{ 1 + i \int_0^l \theta(x) dx \right\} |\beta\rangle_q. \quad (\text{S22})$$

The integrals represent the average value of $\theta(x)$ within each pixel, which is exactly what we need. However, the foregoing argument fails to hold when the conditions $\theta(x) \ll 1$ and $k \ll 2\pi/l$ are not met. For example, large spatial variation of $\theta(x)$ within the pixel should lead to a high deflection angle k/k_z , which results in detection of an electron outside the unscattered beam. Then, the above expansion $e^{i[\theta(x)-kx]} \simeq 1 + i[\theta(x) - kx]$ is itself incorrect since the first term represents the unscattered beam. The absolute value of the two amplitudes ${}_e\langle x|0\rangle_e$ and ${}_e\langle x|1\rangle_e$ at the point of electron detection can be very different because outside the unscattered beam, the wavefunction amplitude strongly depends on the exact form of $\theta(x)$ within the pixel.

V. OBFUSCATION OF ELASTIC SCATTERING

For the reader's convenience, we spell out all the intermediate steps of calculation in the main text that describe obfuscation of elastic scattering. Let the number of pixels of the QAD be M^2 , where M is a multiple of 4. Each pixel,

with the *effective* side length $\sigma = L/M$ measured on the specimen plane, is labeled n, m , where $-M/2 \leq n < M/2$ and likewise for m . Each pixel is associated with the state $|n, m\rangle_d$ of the QAD. The labels n, m respectively correspond to the axes x, y . Let the wavevectors of the incident waves $|s\rangle_e$ and $|a\rangle_e$ projected on the xy -plane be \mathbf{q}_i and $-\mathbf{q}_i$, respectively, where \mathbf{q}_i has only the x -component $q_i = \pi/2\sigma$, i.e. the y -component is zero.

The qubit Q1 is initially in the state

$$|s\rangle_q + i\alpha|a\rangle_q \quad (\text{S23})$$

and after the electron, whose initial state is $\frac{1}{\sqrt{2}}\{|s\rangle_e + |a\rangle_e\}$, goes through Q1, the state of the entire system is

$$\frac{1}{\sqrt{2}}\{(|s\rangle_e|s\rangle_q + |a\rangle_e|a\rangle_q) + i\alpha(|s\rangle_e|a\rangle_q + |a\rangle_e|s\rangle_q)\} \quad (\text{S24})$$

First, the exit wave from the specimen $\{1 + i\theta(x, y)\}e^{i(q_i x + k_z z)}$ (where $q_i \ll k_z$) generated from the incident wave $|s\rangle_e$ is captured by the QAD as a state (the subscript stands for “detector”)

$$|\psi_s\rangle_d = \frac{1}{M} \sum_{n,m} (1 + i\theta_{n,m}) e^{i\frac{\pi}{2}n} |n, m\rangle_d, \quad (\text{S25})$$

where $\theta_{n,m} = \theta(n\sigma, m\sigma)$ and n, m each runs from $-M/2$ to $M/2 - 1$. A similar argument holds for the incident wave $|a\rangle_e$, resulting in

$$|\psi_a\rangle_d = \frac{1}{M} \sum_{n,m} (1 + i\theta_{n,m}) e^{-i\frac{\pi}{2}n} |n, m\rangle_d. \quad (\text{S26})$$

Thus, the state of the entire system is

$$\frac{1}{\sqrt{2}}\{(|\psi_s\rangle_d|s\rangle_q + |\psi_a\rangle_d|a\rangle_q) + i\alpha(|\psi_s\rangle_d|a\rangle_q + |\psi_a\rangle_d|s\rangle_q)\} \quad (\text{S27})$$

Second, we perform 2-dimensional (2d) quantum fast Fourier transform (qFFT) [S14], which converts the amplitude $c_{n,m}$ of the state $|n, m\rangle_d$ to

$$c'_{n,m} = \frac{1}{M} \sum_{n',m'} c_{n',m'} e^{2\pi i \frac{nn' + mm'}{M}} \quad (\text{S28})$$

on the QAD state. This amounts to virtually moving to the diffraction plane. Before proceeding, we define

$$\Theta_{r,s} = \frac{1}{M} \sum_{n,m} \theta_{n,m} e^{2\pi i \frac{rn + sm}{M}}. \quad (\text{S29})$$

Note two properties

$$\Theta_{r+M,s} = \Theta_{r,s} \quad (\text{S30})$$

and

$$\Theta_{r,s} = \Theta_{-r,-s}^*. \quad (\text{S31})$$

When applied respectively to $|\psi_s\rangle_d$ and $|\psi_a\rangle_d$, qFFT yields

$$\begin{aligned} |\psi_{s2}\rangle_d &= \left(1 + \frac{i\Theta_{0,0}}{M}\right) |-\frac{M}{4}, 0\rangle_d + \frac{i}{M} \sum_{(r,s) \neq (-\frac{M}{4}, 0)} \Theta_{r+\frac{M}{4},s} |r, s\rangle_d, \\ |\psi_{a2}\rangle_d &= \left(1 + \frac{i\Theta_{0,0}}{M}\right) |\frac{M}{4}, 0\rangle_d + \frac{i}{M} \sum_{(r,s) \neq (\frac{M}{4}, 0)} \Theta_{r-\frac{M}{4},s} |r, s\rangle_d. \end{aligned} \quad (\text{S32})$$

Henceforth we set $\Theta_{0,0} = 0$, or equivalently, set the average of the phase shift $\theta(x, y)$ to be zero. Define

$$\bar{\theta} \equiv \frac{\Theta_{\frac{M}{2},0}}{M} = \frac{\Theta_{-\frac{M}{2},0}}{M} = \frac{1}{M^2} \sum_{n,m} (-1)^n \theta_{n,m}, \quad (\text{S33})$$

which represents the spatial frequency component we aim to measure. That is, half the difference between (A) the average value of $\theta_{n,m}$ with even n and (B) the odd n counterpart. The state of the entire system is thus

$$\begin{aligned} |\Psi_1\rangle = & \frac{1}{\sqrt{2}} \left| -\frac{M}{4}, 0 \right\rangle_d [(1 - \alpha\bar{\theta}) |s\rangle_q + i(\alpha + \bar{\theta}) |a\rangle_q] + \frac{1}{\sqrt{2}} \left| \frac{M}{4}, 0 \right\rangle_d [(1 - \alpha\bar{\theta}) |a\rangle_q + i(\alpha + \bar{\theta}) |s\rangle_q] \\ & + \frac{i}{\sqrt{2}M} \sum_{(r,s) \neq \pm(\frac{M}{4}, 0)} |r, s\rangle_d \left\{ \Theta_{r+\frac{M}{4},s} (|s\rangle_q + i\alpha|a\rangle_q) + \Theta_{r-\frac{M}{4},s} (|a\rangle_q + i\alpha|s\rangle_q) \right\}. \end{aligned} \quad (\text{S34})$$

Third, we apply a “virtual $\pi/2$ phase plate” by selectively apply a phase factor $-i$ to the all scattered states, i.e. $|r, s\rangle_d$ with $(r, s) \neq \pm(\frac{M}{4}, 0)$, that are in the second line of the above equation.

Fourth, to “obscure” the history of scattering, we apply inverse qFFT (iqFFT) to each of two half planes $M/2 \leq r < 0$ and $0 \leq r < M/2$, that respectively contains unscattered waves $|s\rangle_e$ and $|a\rangle_e$. We carry this out by leaving the most significant qubit (MSQ) representing the coordinate along the x axis when performing iqFFT. Call this qubit Q2. On the other hand, iqFFT is done fully on the all qubit representing the coordinate on y axis.

Two definitions are in order before we proceed. We first introduce

$$\theta_{n,m}^L = \frac{1}{M} \sum_{\substack{-\frac{M}{4} \leq r' < \frac{M}{4}, s \\ (r', s) \neq (0, 0)}} \Theta_{r',s} e^{-2\pi i \frac{2r'n+sm}{M}}, \quad (\text{S35})$$

where we impose the range $-\frac{M}{4} \leq n < \frac{M}{4}$, $-\frac{M}{2} \leq m < \frac{M}{2}$. The addition of the condition $(r, s) \neq (0, 0)$ changes nothing here, but it makes later arguments clearer. This quantity clearly represents a low-pass filtered map of $\theta_{n,m}$, which is compressed in the x -direction. Because the number of pixels along the axis of compression is $M/2$, we have the slightly odd-looking exponent $-2\pi i \frac{r'n}{(M/2)} - 2\pi i \frac{sm}{M} = -2\pi i \frac{2r'n+sm}{M}$. We also introduce

$$\theta_{n,m}^H = \frac{1}{M} \sum_{\substack{-\frac{M}{4} \leq r' < \frac{M}{4}, s \\ (r', s) \neq (0, 0)}} \Theta_{r'+\frac{M}{2},s} e^{-2\pi i \frac{2r'n+sm}{M}}, \quad (\text{S36})$$

which also has the range $-\frac{M}{4} \leq n < \frac{M}{4}$, $-\frac{M}{2} \leq m < \frac{M}{2}$. Note that we subtracted $\bar{\theta}$ by excluding the $(r', s) = (0, 0)$ term (See Eq. (S33)). We list several useful observations on $\theta_{n,m}^L$ and $\theta_{n,m}^H$. (A) Due to Eq. (S30), $\theta_{n,m}^H$ is equivalently expressed as (in terms of $r'' = r' + M/2$)

$$\theta_{n,m}^H = \frac{1}{M} \sum_{\substack{-\frac{M}{2} \leq r'' < -\frac{M}{4} \\ \frac{M}{4} \leq r'' < \frac{M}{2} \\ (r'', s) \neq (-\frac{M}{2}, 0)}} \Theta_{r'',s} e^{-2\pi i \frac{2r''n+sm}{M}}, \quad (\text{S37})$$

which makes it clear that $\theta_{n,m}^H$ represents a high-pass filtered map of $\theta_{n,m}$. Being high-pass filtered, we expect elements of $\theta_{n,m}^H$ to be generally smaller than the low-pass filtered elements $\theta_{n,m}^L$ for most natural images. (B) Equations (S31), (S35) and (S37) tell us that both the objects $\theta_{n,m}^L$, $\theta_{n,m}^H$ are approximately real. (For example, $r' = -M/4$ terms in Eq. (S35) contribute an imaginary part. The influence could be large especially when M is small.) (C) Some further equivalent expressions are

$$\theta_{n,m}^L = \frac{1}{M} \sum_{\substack{-\frac{M}{2} \leq r < 0, s \\ (r, s) \neq (-\frac{M}{4}, 0)}} \Theta_{r+\frac{M}{4},s} e^{-2\pi i \frac{2(r+\frac{M}{4})n+sm}{M}} = \frac{1}{M} \sum_{\substack{0 \leq r < \frac{M}{2}, s \\ (r, s) \neq (\frac{M}{4}, 0)}} \Theta_{r-\frac{M}{4},s} e^{-2\pi i \frac{2(r-\frac{M}{4})n+sm}{M}}, \quad (\text{S38})$$

$$\theta_{n,m}^H = \frac{1}{M} \sum_{\substack{-\frac{M}{2} \leq r < 0, s \\ (r,s) \neq (-\frac{M}{4}, 0)}} \Theta_{r-\frac{M}{4},s} e^{-2\pi i \frac{2(r+\frac{M}{4})n+sm}{M}} = \frac{1}{M} \sum_{\substack{0 \leq r < \frac{M}{2}, s \\ (r,s) \neq (\frac{M}{4}, 0)}} \Theta_{r+\frac{M}{4},s} e^{-2\pi i \frac{2(r-\frac{M}{4})n+sm}{M}}. \quad (\text{S39})$$

Note that Eq. (S30), which is due to the discrete nature of FFT that comes with the use of QC, is crucial in deriving some of the above results, including the real-valuedness. This does not, however, necessarily mean that continuous Fourier transform realized by an electron optical system, as opposed to a QC, cannot approximate the operation to a satisfactory degree.

Going back to the fourth step, first consider the half plane $-\frac{M}{2} \leq r < 0$ and apply iqFFT of the form

$$a_{n,m} = \frac{\sqrt{2}}{M} \sum_{-\frac{M}{2} \leq r < 0, s} A_{r,s} e^{-2\pi i \frac{2(r+\frac{M}{4})n+sm}{M}}, \quad (\text{S40})$$

where the central pixel is $(-\frac{M}{4}, 0)$. This is done on the condition that the Q2 is in the state $|0\rangle_{q2}$ and results in

$$\begin{aligned} & \frac{1}{M} \sum_{n,m} |n,m\rangle_d \{ (1 - \alpha\bar{\theta}) |s\rangle_q + i(\alpha + \bar{\theta}) |a\rangle_q \\ & + [\theta_{n,m}^L (|s\rangle_q + i\alpha|a\rangle_q) + \theta_{n,m}^H (|a\rangle_q + i\alpha|s\rangle_q)] \} \frac{|0\rangle_{q2}}{\sqrt{2}}. \end{aligned} \quad (\text{S41})$$

Likewise, iqFFT on the remaining plane $0 \leq r < \frac{M}{2}$ results in a state

$$\begin{aligned} & \frac{1}{M} \sum_{n,m} |n,m\rangle_d \{ (1 - \alpha\bar{\theta}) |a\rangle_q + i(\alpha + \bar{\theta}) |s\rangle_q \\ & + [\theta_{n,m}^L (|a\rangle_q + i\alpha|s\rangle_q) + \theta_{n,m}^H (|s\rangle_q + i\alpha|a\rangle_q)] \} \frac{|1\rangle_{q2}}{\sqrt{2}}. \end{aligned} \quad (\text{S42})$$

The state of the entire system is the sum of Eqs. (S41) and (S42). This is what we needed to show.

The setting $q_i = \pi/2\sigma$ entails a problem at lower resolution measurements because high-spatial-frequency component may be present *within* the large pixel of size σ . See the last paragraph of Sec. IV. Detailed discussion of this issue would lead us too far afield because our scheme must be significantly extended to properly take care of this type of error. One solution is to set $q_i = \pi/4\sigma$ and use 4 electron states $|0\rangle_e, \dots, |3\rangle_e$ instead of the two states $|s\rangle_e$ and $|a\rangle_e$. We defer detailed discussion of this extended scheme to future publication.

VI. INFLUENCE OF LARGE BACKGROUND PHASE IN CONVENTIONAL ELECTRON MICROSCOPY

Consider a specimen with a square waveform structure, associated with phase shift periodically switching between δ and $-\delta$. When observed with in-focus phase contrast microscopy, the probabilities to detect an electron at the two regions corresponding respectively to phase shift $\pm\delta$ are

$$\begin{aligned} p_{\pm} &= F |e^{\pm i\delta} - 1 + i|^2 = F (3 - 2 \cos \delta \pm 2 \sin \delta) \\ &= \frac{1}{2} \pm \frac{\sin \delta}{3 - 2 \cos \delta} \simeq \frac{1}{2} \pm \frac{\delta}{1 + \delta^2}, \end{aligned} \quad (\text{S43})$$

where the constant $F = 1/(6 - 4 \cos \delta)$ ensures $p_+ + p_- = 1$. Suppose that there is a smaller variation $d\delta$ on top of the $+\delta$ part. The change of contrast due to $d\delta$ is proportional to

$$\frac{dp_+}{d\delta} = \frac{3 \cos \delta - 2}{(3 - 2 \cos \delta)^2} \simeq 1 - \frac{7\delta^2}{2}. \quad (\text{S44})$$

On the other hand, the noise level is proportional to (as we are dealing with the Bernoulli distribution)

$$\sqrt{p_+ p_-} = \sqrt{\frac{1}{4} - \left(\frac{\sin \delta}{3 - 2 \cos \delta} \right)^2} \simeq \frac{1}{2} - \delta^2. \quad (\text{S45})$$

Hence signal-to-noise ratio decreases as a function proportional to $1 - 3\delta^2/2$ when there is a “background phase” δ .

VII. PRELIMINARY REMARKS ON INCOHERENCE OF INELASTICALLY SCATTERED ELECTRONS

An electron that undergoes inelastic scattering loses coherence to some degree. This is due to generation of (most likely non-maximal) entanglement between the imaging electron and degrees of freedom in the specimen upon scattering. As noted in the main text, the relevant degrees of freedom here are considered to be plasmons. Generation of entanglement results in a mixed state, as opposed to a pure state, of the scattered imaging electron. For the purpose at hand, however, we can project the quantum state of the specimen's degrees of freedom to one of a set of orthogonal basis states (or, loosely speaking, we "measure" the quantum state of the specimen's degrees of freedom). We then find what would be left, as a state of the imaging electron.

Although the relevant excitation is plasmons in the present context, we employ a hydrogenic model for the present preliminary analysis. The ejection process of K-shell electrons has been studied by Maslen and Rossouw (MR) in a hydrogenic scattering model long ago [S15]. Here we evaluate the process using the energy loss value $\Delta E = 20\text{ eV}$ relevant to plasmon excitations, instead of the value $\Delta E = 300\text{ eV}$ used in the original work [S15]. We rather arbitrarily set the binding energy value $E_b = 5\text{ eV}$ of the electron that is to be ejected, whereas in the original work the value of carbon K edge $E_b = 285\text{ eV}$ was used as the binding energy. In what follows, we use notations in Ref.[S15].

In the MR model, the imaging electron is deflected by an angle θ . The wavevector κ of the ejected 15 eV electron is generally different from the scattering vector $\mathbf{q} = \mathbf{k}_f - \mathbf{k}_i$. Let the angle between the vectors κ and \mathbf{q} be γ . As always in the present work, the magnitude of incident electron's wavevector \mathbf{k}_i and the velocity v correspond to those of 300 keV electrons. We set the relevant atomic number Z to be 6, i.e. that of carbon. The atomic transition matrix M_{if} , to which the electron scattering amplitude $f(\theta)$ is proportional, can be computed analytically as a complex function of Z , $\kappa = |\kappa|$, γ and $q = |\mathbf{q}|$ [S15]. Note that θ is a function of some of these parameters. Being complex, the matrix element M_{if} has a phase angle. We take a part of the angle ψ that is dependent on θ and γ ($\psi_2 + \psi_3$ in Ref.[S15]). Figure S3 shows ψ and $|M_{if}|^2$ as functions of $0 \leq \gamma \leq \pi$ for 4 values of θ .

Suppose that we "measured" the ejected 15 eV electron and determined the angle γ to be close to zero. Figure S3 (b) shows that this γ value is rather likely, judging from the broad peak at near $\gamma = 0$ (in spite of a geometric factor $\sin \gamma$ appearing in the total cross section [S15]). On the other hand, Fig. S3 (a) shows that at near $\gamma = 0$, the "phase spread" of 4 curves is about 0.5 radian. More generally, the scattered electron wave

$$\Psi(\theta) \propto \frac{1}{\sqrt{\theta^2 + \theta_E^2}}, \quad (\text{S46})$$

where

$$\theta_E = \sqrt{1 - (v/c)^2} \frac{\Delta E}{mv^2} = 41\text{ }\mu\text{rad}, \quad (\text{S47})$$

receives phase modulation. This modulation may roughly be modeled as $e^{i\psi(\theta)} \simeq e^{i\zeta\theta/\theta_c}$, where $\theta_c = \sqrt{2\theta_E} = 9.1\text{ mrad}$ is the Bethe-ridge [S16]. The parameter ζ , which depends on the direction of the electron ejection γ , appears to be in between 0.1 and 0.5 for $\theta < 10\text{ mrad}$ (See Fig. S3 (a)) unless γ is close to, but not exactly at, $\frac{\pi}{2}$. The event $\gamma \simeq \frac{\pi}{2}$ appears to be relatively unlikely (See Fig. S3 (b)).

On the other hand, the correction factor, due to incoherence of inelastic scattering, to the Ivanovic-Dieks-Peres failure probability is essentially given by the absolute value of the inner product

$$I = " \langle \Psi(\theta) | \Psi(\theta) e^{i\zeta\theta/\theta_c} \rangle " = \int_0^{\theta_c} \Psi^2(\theta) e^{i\zeta\theta/\theta_c} 2\pi\theta d\theta. \quad (\text{S48})$$

The part inside the quotation marks merely shows the idea and therefore is schematic. We find $I = 1 - 10^{-4}$ for $\zeta = 0.1$ and $I = 0.97$ for $\zeta = 1$. These values appear to be sufficiently close to 1. Nonetheless, it goes without saying that further study, which for instance evaluates the failure probability due to $\gamma \simeq \frac{\pi}{2}$ events, or one which takes into account the plasmonic nature of the excitation etc., is desirable.

VIII. OVERLAP OF THE INELASTICALLY SCATTERED STATES $|s'\rangle_e$ AND $|a'\rangle_e$

The calculation of $p_f(\beta)$ is carried out as follows. We express the scattering angle β as

$$\beta^2 = \beta_x^2 + \beta_y^2, \quad (\text{S49})$$

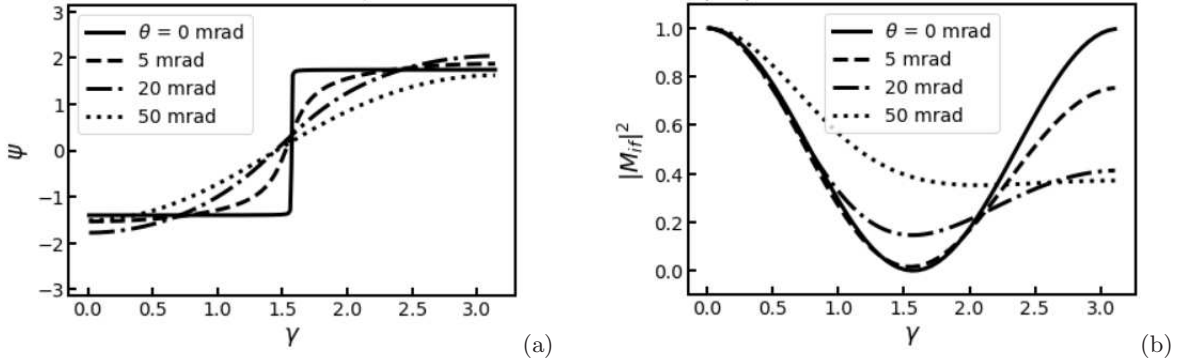


FIG. S3: Quantities pertaining to the atomic transition matrix M_{if} discussed in the model of Maslen-Rossouw. (a) The phase angle component $\psi = \psi_2 + \psi_3$ of M_{if} is shown, which depends on the angle of scattering θ and γ . This plot corresponds to Fig. 6 of Ref. [S15] computed for K-shell electron ejection processes. (b) The squared amplitude $|M_{if}|^2$ tends to be small at $\gamma \simeq \frac{\pi}{2}$.

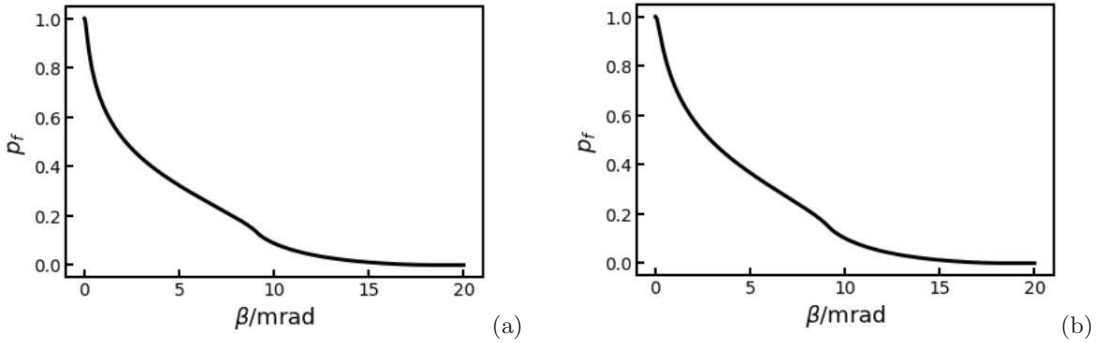


FIG. S4: Two $p_f(\beta)$ curves respectively for (a) $\Delta E = 20$ eV and (b) $\Delta E = 40$ eV.

in terms of the x, y components of the angle. Inelastically scattered electron waves have an amplitude proportional to

$$f(\beta_x, \beta_y) = \begin{cases} (\beta_x^2 + \beta_y^2 + \beta_E^2)^{-1/2} & \beta_x^2 + \beta_y^2 < \beta_c^2 \\ 0 & \beta_x^2 + \beta_y^2 > \beta_c^2 \end{cases} \quad (\text{S50})$$

where $\beta_c = 9.1$ mrad and $\beta_E = 41 \mu\text{mrad}$ is proportional to the energy loss ΔE , which is taken as 20 eV here. The function $p_f(\beta)$ is 2d-autocorrelation of the function $f(\beta_x, \beta_y)$. Specifically,

$$p_f(\beta) = F \int d\beta_x \int d\beta_y f(\beta_x, \beta_y) f(\beta - \beta_x, \beta_y), \quad (\text{S51})$$

where the normalization constant F is adjusted so that $p_f(0) = 1$, i.e. the failure probability is $p_f = 1$ when the two scattered waves are the same. Autocorrelation translates to multiplication when (inverse-)Fourier transformed. Hence we obtain

$$p_f(\beta) \propto \mathcal{F} \left\{ [\mathcal{F}^{-1} \{ f(\beta_x, \beta_y) \}]^2 \right\} (\beta, 0). \quad (\text{S52})$$

We computed $\mathcal{F}^{-1} \{ f(\beta_x, \beta_y) \}$ numerically.

To show the sensitivity of the curve $p_f(\beta)$ to the energy loss ΔE , we show two cases, $\Delta E = 20$ eV (which is regarded as typical) and $\Delta E = 40$ eV in Fig. S4.

We remark on the point in the main text that the incident electron beams $|s\rangle_e$ and $|a\rangle_e$ should be sufficiently parallel. The curve $p_f(\beta)$ in Fig. 2 of the main text is computed for the two plane wave beams $|s\rangle_e$ and $|a\rangle_e$. We call this case the plane-wave beam case (PBC). Also consider the case in which the angular spread of the incident wave functions $|s\rangle_e$ and $|a\rangle_e$ (not the intensity) is $e^{-\beta^2/2\beta_g^2}$. We call this the divergent beam case (DBC), although the beam may instead be convergent. In the DBC, the scattered wave in the far field is convolution of $f(\beta_x, \beta_y)$

and $e^{-(\beta_x^2 + \beta_y^2)/2\beta_g^2}$. Hence the DBC exit wave on the image plane is the PBC exit wave multiplied by $e^{-\frac{\beta_g^2}{2}(x^2 + y^2)}$. Thus, the intensity of the DBC exit wave is equal to the PBC exit wave multiplied by $e^{-\beta_g^2(x^2 + y^2)}$. Since the error probability $p_f(\beta)$ is Fourier transform of the square of the exit wave, we see that the DBC version of $p_f(\beta)$ equals convolution of the PBC version of $p_f(\beta)$ and

$$e^{-(\beta_x^2 + \beta_y^2)/4\beta_g^2} \propto \mathcal{F} \left\{ e^{-\beta_g^2(x^2 + y^2)} \right\}. \quad (\text{S53})$$

In other words, the DBC version of $p_f(\beta)$ is obtained by applying the gaussian low-pass filter $\propto e^{-(\beta_x^2 + \beta_y^2)/4\beta_g^2}$ to the PBC version of $p_f(\beta)$. Because of the normalization condition $p_f(0) = 1$, a larger β_g gives rise to poorer QEM performance because the peak of $p_f(\beta)$ at $\beta = 0$ is smeared due to low-pass filtering. On the other hand, reducing β_g much beyond $\beta_E \simeq 40\mu\text{rad}$ is unnecessary as suggested by the form of $p_f(\beta)$ at near $\beta = 0$, which comes from the form of $f(\beta_x, \beta_y)$ at near $\beta = 0$.

IX. COMPUTING THE PHASE MAP

We computed the phase map (Fig. S1(a)) of the Marburg virus VP35 oligomerization domain (5TOI) [S5] using the multislice algorithm. The thickness of each slice is 1 nm. A simpler simulation using the projection assumption [S2] gave very similar results, which is not surprising because the thickness of the 5TOI molecule is as thin as $\simeq 3$ nm.

The handling of water molecules surrounding the 5TOI molecule closely followed the method described by Shang and Sigworth [S17]. Here we only describe places where we made deviations from their method when we took the surrounding water molecules into account. Following the main text, we focus on 300 keV electrons. All computations were carried out on a Cartesian grid with a grid spacing 0.05 nm. The shape of the space was cubic with the volume $V = L^3$, where $L = 12.0$ nm.

First, we remark that the surrounding water structure is not *obviously* averaged out under the assumption of single image acquisition in the present work, unlike in the context of SPA considered in Ref. [S17]. However, there is evidence that water molecules move significantly during the electron exposure [S3]. Here we assume that the use of averaged-out water density is justified.

We computed the inner potentials for relevant elements H, C, N, O and S as follows. The scattering amplitudes $f(\theta)$ at $\theta = 0$ for the elements were obtained from a NIST database [S4]. From these values we computed the values of inner potentials V_i (which has the dimension of voltage times volume) as

$$V_i = \sqrt{1 - \left(\frac{v}{c}\right)^2} \frac{2\pi\hbar^2}{me} f(0), \quad (\text{S54})$$

where m and v are the electron mass and velocity, respectively. Table I shows the result.

The mean inner potential of ice is computed to be 4.5276 V. In other words, this value represents the inner potential of the water molecule, consisting of 2 hydrogen atoms and one oxygen atom, divided by its molecular volume in ice. There is a discrepancy in the literature regarding the exact value of it. Reference [S17] reports 3.6 V for “bulk vitreous ice”, whereas Ref. [S18] reports a value 4.5301 V for “low-density amorphous ice” (LDA ice). Under the assumption that the density of LDA ice $9.3 \times 10^2 \text{ kg/m}^3$ is relevant, the latter value, which is consistent with our result, is more appropriate.

The “atomic radii” used for computing the “binary mask function” $m(\mathbf{r})$ [S17] are shown in Table II. We use van der Waals (VDW) radii taken from Table 2 of Ref. [S19] for this purpose. To be precise, the VDW radii depends on the atomic group to which the atom belongs. However, we simply averaged all values appearing in the “ProtOr Radii” column of the Table 2 of Ref. [S19]. This is clearly a crude approximation but we believe that the associated error is insignificant for the present purpose of evaluating QEM.

The area of the molecule $\hat{A} = 23 \text{ nm}^2$, mentioned in Sec. I, was computed using the mask function $m(\mathbf{r})$. The function is designed to indicate whether or not a location \mathbf{r} is inside the molecule, in such a way that $m(\mathbf{r}) = 0$ if \mathbf{r} is inside the molecule and $m(\mathbf{r}) = 1$ otherwise. Hence we computed

$$\hat{A} = \int \int dx dy H \left(\frac{1}{L} \int \{1 - m(\mathbf{r})\} dz \right), \quad (\text{S55})$$

where z is the optical axis, and the version of the Heaviside step function $H(X)$ employed here is left-continuous, i.e. $H(0) = 0$. The length L is inserted solely for making the argument of the function dimensionless.

Hydrogen requires a special treatment. Atomic coordinates for the hydrogen atoms are absent in the PDB, for the Marburg virus VP35 oligomerization domain (5TOI). Following the general strategy described in Ref. [S17], we

TABLE I: The inner potential V_i (multiplied by the volume).

Element	H	C	N	O	S
$V_i/\text{V nm}^3$	0.0253	0.118	0.106	0.095	0.246

TABLE II: Atomic radii a_i .

Element	H	C	N	O	S
a_i/nm	0	0.180	0.164	0.144	0.177

modified the inner potential values of C, N, O and S atoms in accordance with the expected number of the associated H atoms to each of these elements. We computed the expected values as weighted-average of the number of hydrogen atoms in each type of amino-acid residue, over all residue types with weights in accordance with the frequency of each residue in the 5TOI molecule.

X. COMPUTATION OF IMAGE NOISE

Here we describe the procedure to generate simulated images shown in Fig. 3 in the main text. The map of phase shift shown in Fig. 3 (a) is produced as described in Sec. IX. All computations are performed on 240×240 pixels image data, with each square pixel having the side length $l = 0.05 \text{ nm}$. We label each pixel with a pair of integers (n, m) , each of which ranges from -120 to 119 .

To simulate imaging processes, we add the expected noise to the phase map to produce Figs. 3 (b)-(f). Typically, although not always, many quantum measurements, each involving k electron passing events, are performed for each pixel. Hence we expect the noise to be approximately gaussian. In all three of the imaging methods the amount of noise depends on the transverse wave vector component $q = k_z \beta$, where k_z is the wave number along the optical axis.

First, we generate real-valued, independent gaussian noise, with zero mean and unit variance, in each pixel on the image plane. Second, we perform fast Fourier transform (FFT) to obtain the noise in the diffraction plane, which results in a complex-valued map. The pixel $(0, 119)$ in the map, for example, corresponds to a scattering angle

$$\beta \simeq \sin \beta = \frac{\lambda}{2l} = \frac{1.97 \text{ pm}}{2 \times 0.05 \text{ nm}} \times \frac{119}{120} = 19.5 \text{ mrad}, \quad (\text{S56})$$

where $\lambda = 2\pi/k_z \simeq 1.97 \text{ pm}$ is the wavelength of 300 keV electrons. Third, to the map on the diffraction plane we multiply a function that describes the q -dependent amplitude of noise. For the “classical” case of Fig. 3 (b), we multiply the standard deviation of shot noise

$$\frac{1}{\sqrt{N_{sq}}} = \frac{1}{\sqrt{F_{sq}A}} = \sqrt{\frac{Rq^4}{128\pi^5\gamma}} = \sqrt{\frac{R}{128\pi^5\gamma}} \frac{q^2}{k_z^2} k_z^2 = \frac{10^{-6}}{2\lambda^2} \sqrt{\frac{R}{2\pi\gamma}} \left(\frac{\beta}{\text{mrad}}\right)^2 = \frac{(\beta/\text{mrad})^2}{186}, \quad (\text{S57})$$

where $\gamma = 0.064$ as described in Sec. III. (Uncertainties associated with parameters such as R, γ do not warrant the precision appearing in the numerical value 186, but we use this value in the simulation anyway.) Note, by convention, that the square of Eq. (S57) equals

$$S_n(\beta) \Delta q^2 = S_n(\beta) \frac{(2\pi)^2}{A}, \quad (\text{S58})$$

where $S_n(\beta)$ is the noise power spectrum per unit “area” in the reciprocal space. The images shown in Figs. 3 (c)-(f) have smaller noise due to quantum enhancement. The factors of noise reduction, $\sqrt{e/k_1}$ and $\sqrt{ep_f(\beta)/k_2}$ respectively, are noted in the main text, along with the definitions $k_1 = \min(k, N_{sq})$ and $k_2 = \min(k/p_f(\beta), N_{sq})$. Fourth and finally, we apply inverse-FFT (iFFT) to obtain spatial-frequency-weighted noise patterns. The result should mathematically be real, but the real part should be taken in numerical computation. The resultant noise patterns are simply added to the phase map, i.e. $\theta(x, y)$ of the exit wave $1 + i\theta(x, y)$ (Fig. 3 (a)) to obtain Figs. 3 (b)-(f).

The contrast of all images Fig. 3 (a)-(f) are adjusted in the following way. Given a numerical array representing an image, the mean μ and the standard deviation σ are computed. The highest and the lowest brightness in each presented image are then made to correspond to the values $\mu + 5\sigma$ and $\mu - 5\sigma$, respectively. Finally, the images are cropped to the size of approximately 80×200 pixels for presentation.

XI. CONVENTIONAL WEAK-PHASE MEASUREMENT

To clarify the point mentioned in Sec. III, we consider a weak-phase object and compare the abilities of various measurement schemes. It turns out that, among in-focus phase contrast imaging (with a $\pi/2$ phase plate), dark field imaging, far-field diffraction measurement, none is more advantageous than others in terms of phase measurement precision, if we put aside the ability to decide the sign of the small phase under measurement. We also show that discretized and scanning versions of phase contrast imaging have essentially the same limitation. Many of these facts have long been known [S20], but it is instructive to explicitly derive these. Note that the equivalence among these methods does not mean that all measurement schemes have the equal ability. Considering in-focus bright field imaging without a phase plate should suffice to see this point. Also note that, although the followings are presented in terms of conventional TEM, the results extends also to QEM because in a sense QEM is essentially the same method: The “only difference” is that QEM employs a hypothetical particle instead of the electron, which damages the specimen k times more than the electron, while receiving k times larger phase shift upon passing the specimen.

Let the exit wave function emanating from a biological weak-phase object be

$$\psi(\mathbf{r}) = \frac{1}{\sqrt{2\pi\sigma^2}} e^{-\frac{x^2+y^2}{4\sigma^2}} e^{ik_z z} \{1 + i\theta(x, y)\}, \quad (\text{S59})$$

where $\theta(x, y) \ll 1$, $\int dx \int dy \theta(x, y) = 0$ and σ^2 is roughly the area of the illuminating electron beam. Define

$$\Theta(k_x, k_y) = \mathcal{F}\{\theta(x, y)\} = \int dx \int dy \theta(x, y) e^{-i(k_x x + k_y y)}. \quad (\text{S60})$$

Let $*$ be the convolution operator, which in the reciprocal space is

$$(F * G)(k_x, k_y) = \int \frac{dl_x}{2\pi} \int \frac{dl_y}{2\pi} F(l_x, l_y) G(k_x - l_x, k_y - l_y). \quad (\text{S61})$$

The probability distributions for electron detection are respectively as follows. The distribution for in-focus phase contrast mode is

$$P_1(x, y) = \frac{1}{2\pi\sigma^2} e^{-\frac{x^2+y^2}{2\sigma^2}} \{1 + 2\theta(x, y)\}. \quad (\text{S62})$$

In the dark field mode, the distribution is

$$P_2(x, y) = \frac{1}{2\pi\sigma^2} e^{-\frac{x^2+y^2}{2\sigma^2}} \theta^2(x, y). \quad (\text{S63})$$

In the case of diffraction pattern measurement we have

$$P_3(k_x, k_y) = \left| \sqrt{8\pi\sigma^2} e^{-\sigma^2(k_x^2+k_y^2)} * \left\{ (2\pi)^2 \delta(k_x) \delta(k_y) + i\Theta(k_x, k_y) \right\} \right|^2, \quad (\text{S64})$$

which is normalized as

$$\int \frac{dk_x}{2\pi} \int \frac{dk_y}{2\pi} P_3(k_x, k_y) = 1. \quad (\text{S65})$$

First, we show the equivalence between in-focus phase contrast imaging and dark field imaging with regard to phase precision. Consider a small area $dxdy$ at a point (x, y) , in which $P_1(x, y)$ and $P_2(x, y)$ are smooth. The probabilities to detect an electron in the area are respectively $p_1 = \alpha \{1 + 2\theta(x, y)\}$ and $p_2 = \alpha\theta^2(x, y)$, where

$$\alpha = \frac{1}{2\pi\sigma^2} e^{-\frac{x^2+y^2}{2\sigma^2}} dxdy. \quad (\text{S66})$$

We illuminate the specimen with N electrons. Let X_n ($n = 1, 2$) be random variables for the number of electrons associated with the probabilities p_n . Let \bar{X}_n and $\text{Var}(X_n)$ be their mean and variance, respectively. We obtain, assuming $\alpha \ll 1$ (if not, take a smaller area $dxdy$)

$$\text{Var}(X_1) = Np_1(1 - p_1) \simeq Np_1 = N\alpha \{1 + 2\theta(x, y)\} \simeq N\alpha, \quad (\text{S67})$$

and

$$\text{Var}(X_2) = Np_2(1 - p_2) \simeq Np_2 = N\alpha\theta^2(x, y). \quad (\text{S68})$$

Also note that $\text{Var}(X_1) \simeq \overline{X_1}$ and $\text{Var}(X_2) \simeq \overline{X_2}$ under this approximation. Using maximum likelihood estimation, the parameter $\theta(x, y)$ is estimated with $Y_1 = \frac{1}{2}(\frac{X_1}{N\alpha} - 1)$ and $Y_2 = \sqrt{X_2/N\alpha}$. We obtain

$$\text{Var}(Y_1) \simeq \frac{1}{4N\alpha}. \quad (\text{S69})$$

Obtaining $\text{Var}(Y_2)$ takes some steps. We begin with

$$\begin{aligned} Y_2 &= \sqrt{\frac{X_2}{N\alpha}} = \sqrt{\frac{(X_2 - \overline{X_2}) + \overline{X_2}}{N\alpha}} = \sqrt{\frac{\overline{X_2}}{N\alpha}} \sqrt{1 + \frac{X_2 - \overline{X_2}}{\overline{X_2}}} \\ &\simeq \sqrt{\frac{\overline{X_2}}{N\alpha}} \left(1 + \frac{X_2 - \overline{X_2}}{2\overline{X_2}} \right) = \theta(x, y) \left\{ 1 + \frac{X_2 - \overline{X_2}}{2\overline{X_2}} \right\}. \end{aligned} \quad (\text{S70})$$

Our calculation is accurate to the extent that the approximation in the above formula is accurate. (One expects $\frac{X_2 - \overline{X_2}}{X_2} \simeq \frac{1}{\sqrt{N\alpha}\theta}$.) Hence

$$\text{Var}(Y_2) \simeq \overline{(Y_2 - \theta(x, y))^2} = \theta^2(x, y) \frac{\overline{(X_2 - \overline{X_2})^2}}{4\overline{(X_2)^2}} = \theta^2(x, y) \frac{\text{Var}(X_2)}{4\overline{(X_2)^2}} \simeq \frac{1}{4N\alpha}. \quad (\text{S71})$$

Thus, in-focus phase contrast imaging and dark field imaging has essentially the same precision for a given electron fluence. However, the former can detect the sign of $\theta(x, y)$, while the latter cannot.

Second, we show the equivalence between dark field imaging and intensity measurement at the diffraction plane. Ignoring the unscattered beam in $P_3(k_x, k_y)$ and we are left with

$$P'_3(k_x, k_y) = \left| \sqrt{8\pi\sigma^2} e^{-\sigma^2(k_x^2 + k_y^2)} * \Theta(k_x, k_y) \right|^2. \quad (\text{S72})$$

To simplify the calculation, we only consider a σ much larger than the resolution of interest. Note that $4\pi\sigma^2 e^{-\sigma^2(k_x^2 + k_y^2)} \rightarrow (2\pi)^2 \sigma^2 \delta(\sigma k_x) \delta(\sigma k_y)$ when $\sigma k \gg 1$, where k is the largest spatial angular frequency of interest (we keep the quantity in the delta functions dimensionless). Hence we obtain

$$P'_3(k_x, k_y) \simeq \frac{1}{2\pi\sigma^2} |\Theta(k_x, k_y)|^2. \quad (\text{S73})$$

By Parseval's theorem we have

$$\frac{1}{2\pi\sigma^2} \int \frac{dk_x}{2\pi} \int \frac{dk_y}{2\pi} |\Theta(k_x, k_y)|^2 = \frac{1}{2\pi\sigma^2} \int dx \int dy |\theta(x, y)|^2. \quad (\text{S74})$$

Note that

$$\frac{1}{2\pi\sigma^2} \left(\frac{dk_x}{2\pi} \right) \left(\frac{dk_y}{2\pi} \right) |\Theta(k_x, k_y)|^2 \quad (\text{S75})$$

is the probability to detect an electron in the “area” $dk_x dk_y$ on the diffraction plane. As this probability is small, this also equals the variance associated with it. Likewise, from Eq. (S63) we see that

$$\frac{1}{2\pi\sigma^2} dx dy |\theta(x, y)|^2 \quad (\text{S76})$$

is the probability to find an electron in the area $dx dy$ on the image plane in dark field imaging when the point (x, y) is well within the incident beam. As in the diffraction plane case (Eq. (S75)), Eq. (S76) also represents the variance of the probabilistic process. Therefore, Eq. (S74) tells us that only a redistribution of signal *and* noise occurs when we detect electrons at a diffraction plane, as may be obvious in hindsight. It is in this sense that diffraction pattern measurement is equivalent to the other two in terms of phase measurement precision.

Third, we discretize the image. Let the image have n pixels indexed by $s = 1, 2, \dots, n$. Let the quantum state of an imaging electron localized on the s -th pixel be $|s\rangle$. The small phase shift caused by the specimen is such that the transmitted electron wave emerging from the specimen is described as

$$|\psi\rangle = \frac{1}{\sqrt{n}} \sum_{s=1}^n (1 + i\theta_s) |s\rangle = \frac{1}{\sqrt{n}} \sum_{s=1}^n |s\rangle + \frac{i}{\sqrt{n}} \sum_{s=1}^n \theta_s |s\rangle, \quad (\text{S77})$$

where we adjust the global phase so that $\sum_{s=1}^n \theta_s = 0$. The Fourier transformed state is on the diffraction plane. The state at the center of the diffraction plane corresponds to the first term of the last expression in Eq. (S77), to which we apply a $\pi/2$ phase shift using a phase plate. Hence we obtain, up to the overall phase,

$$|\psi'\rangle = \frac{1}{\sqrt{n}} \sum_{s=1}^n (1 + \theta_s) |s\rangle. \quad (\text{S78})$$

This leads to the probability to find an electron in the state $|s\rangle$, which is $p_s = (1 + 2\theta_s)/n$. Let the random variable describing the number of electrons detected in the s -th pixel be Z_s , when we detect N electrons in total. The variance associated with the detection of an electron is

$$\text{Var}(Z_s) = N p_s (1 - p_s) \simeq \frac{N}{n} \left(1 - \frac{1}{n}\right), \quad (\text{S79})$$

which is a property of the multinomial distribution. This is approximately $N p_s \simeq N/n$ when $n \gg 1$. On the other hand, $W_s = \frac{1}{2} \left(\frac{n}{N} Z_s - 1 \right)$ gives $\theta_s = \overline{W_s}$. We obtain

$$\text{Var}(W_s) = \frac{n}{4N} \left(1 - \frac{1}{n}\right) = \frac{n-1}{4N}. \quad (\text{S80})$$

This is consistent with Eq. (S69) when $n \gg 1$, as it should. Note that $\text{Var}(W_s) = 1/4N$ in the specific case $n = 2$ as in Sec. III.

Fourth, we consider a “scanning” scheme to connect to the arguments in Sec. III. The amount of phase shift θ_s at each pixel, relative to the global average $\sum_{s=1}^n \theta_s = 0$, is measured in the above discrete scheme. Instead, we may split the electron beam and scan one branch of the beam while the other is focused on pixel 1. In this way we measure the phase difference $\theta_s - \theta_1$, where θ_1 is treated as a reference. There are $n - 1$ such measurements and for a fair comparison we use $\frac{N}{n-1}$ electrons for each measurement. Each measurement may be seen as the $n = 2$ case described in the discretized phase contrast imaging. Hence the variance of the measurement is $\frac{n-1}{4N}$. This is exactly the same as $\text{Var}(W_s)$ in the previous discretized case described in the preceding paragraph. Hence the two methods are essentially the same. (Another possibility is to measure a phase difference $\theta_{s+1} - \theta_s$ between each adjacent pair of pixels. This may better represent what should be called a “scanning method”, but is also associated with a larger accumulated error in, e.g. $\theta_n - \theta_1$.)

Finally, we clarify a potentially confusing point. The analysis presented here is applicable also to QEM in the sense mentioned at the outset of this section. We also showed in the preceding paragraph that the scanning method gives essentially the same measurement precision as multi-pixel phase contrast measurement. At first glance, this may appear at odd with the known result [S21] that multi-pixel coherent quantum measurement over n pixels of phase object is superior to a set of Heisenberg-limited single phase measurements, indeed by a factor $\mathcal{O}(n)$ in terms of the total variance. However, in the argument of Ref. [S21], which is correct, the total number of electrons N is fixed. Here is a simple version of the argument: In classical measurement, the number of electrons used for each pixel is N/n and hence the associated variance per pixel is n/N . For the purpose at hand, we may consider multi-pixel quantum measurement simply as electrons passing a multi-pixel specimen N times as in multi-pass TEM [S22], where all N *passages* of a single electron are employed to reach the variance at the Heisenberg limit $\simeq n/N^2$ per pixel, because this should be better than the classical case by a factor N (i.e. the phase is accumulated N times *in each pixel*). On the other hand, if we measure each single pixel separately, but at the Heisenberg limit, each measurement can use only N/n electron passages to reach the corresponding variance at the Heisenberg limit $\simeq n^2/N^2$ per pixel. Hence we conclude that the multi-pixel version of quantum measurement gives a smaller variance by the factor n compared to a set of n single pixel quantum measurements. However, in QEM and possibly in many other applications, the number of passages one can employ is limited to a fixed number s that depends on inelastic scattering, particle loss, dissipation etc. Hence, it should be more appropriate to assign the same number of passages s to both multi-pixel measurement case and the case of a set of single pixel measurements in applications such as QEM. If we do this, then

the aforementioned advantage disappears.

[S1] P. B. Rosenthal and R. Henderson, Optimal determination of particle orientation, absolute hand, and contrast loss in single-particle electron cryomicroscopy, *J. Mol. Biol.* **333**, 721-745 (2003).

[S2] P. Rez, Comparison of phase contrast transmission electron microscopy with optimized scanning transmission annular dark field imaging for protein imaging, *Ultramicroscopy* **96**, 117-124 (2003). Also see Appendix A in: H. Okamoto, Adaptive quantum measurement for low-dose electron microscopy, *Phys. Rev. A* **81**, 043807 (2010).

[S3] G. McMullan, K. R. Vinothkumar, and R. Henderson, Thon rings from amorphous ice and implications of beam-induced Brownian motion in single particle electron cryo-microscopy, *Ultramicroscopy* **158**, 26-32 (2015).

[S4] A. Jablonski, F. Salvat, and C. J. Powell, NIST Electron Elastic-Scattering Cross-Section Database, Version 3.1, National Institute of Standards and Technology, Gaithersburg, MD (2003).

[S5] J. F. Bruhn, R. N. Kirchdoerfer, S. M. Urata, S. Li, I. J. Tickle, G. Bricogne, and E. Ollmann Saphire, Crystal structure of the Marburg virus VP35 oligomerization domain, *J. Virol.* **91**, e01085-16 (2017).

[S6] R. Milo, R. Phillips, and N. Orme, *Cell Biology by the numbers*, (Garland Science, 2016), p. 45.

[S7] S. Subramaniam, R. Henderson, Molecular mechanism of vectorial proton translocation by bacteriorhodopsin, *Nature* **406**, 653-657 (2000).

[S8] K.H. Choi, A. S. Mazurkie, A. J. Morris, D. Utheza, D. R. Tolan, and K. N. Allen, Structure of a fructose-1,6-bis(phosphate) aldolase liganded to its natural substrate in a cleavage-defective mutant at 2.3 Å, *Biochemistry* **38**, 12655-12664 (1999).

[S9] M. J. Peet, R. Henderson, and C. J. Russo, The energy dependence of contrast and damage in electron cryomicroscopy of biological molecules, *Ultramicroscopy* **203**, 125-131 (2019).

[S10] H. Okamoto, Quantum interface to charged particles in a vacuum, *Phys. Rev. A* **92**, 053805 (2015).

[S11] R. Schroeder, B. Barton, H. Rose, and G. Benner, G. Contrast enhancement by anamorphotic phase plates in an aberration-corrected TEM, *Microsc. Microanal.* **13** (Suppl. 3), 8-9 (2007).

[S12] H. H. Rose, Future trends in aberration-corrected electron microscopy, *Philos. Trans. R. Soc. A* **367**, 3809-3823 (2009).

[S13] H. Okamoto, Full-vortex flux qubit for charged-particle optics, *Phys. Rev. A* **97**, 042342 (2018).

[S14] D. R. Simon, On the power of quantum computation, *SIAM J. Comput.*, **26**, 1474-1483 (1997).

[S15] V. W. Maslen and C. J. Rossouw, The inelastic scattering matrix element and its application to electron energy loss spectroscopy, *Phil. Mag. A* **126**, 119-130 (1983).

[S16] R. F. Egerton, Calculation, consequences and measurement of the point spread function for low-loss inelastic scattering, *Microscopy*, **67**, i52-i59 (2018).

[S17] Z. Shang and F. J. Sigworth, Hydration-layer models for cryo-EM image simulation, *J. Struct. Biol.* **180**, 10-16 (2012).

[S18] M. Vulovic, R. B. Ravelli, L. J. van Vliet, A. J. Koster, I. Lazic, U. Lucken, H. Rullgard, O. Oktem, and B. Rieger, Image formation modeling in cryo-electron microscopy, *J. Struct. Biol.* **183**, 19 (2013).

[S19] J. Tsai, R. Taylor, C. Chothia, and M. Gerstein, The packing density in proteins: standard radii and volumes, *J. Mol. Biol.* **290**, 253-266 (1999).

[S20] R. Henderson, The potential and limitations of neutrons, electrons and X-rays for atomic resolution microscopy of unstained biological molecules, *Quart. Rev. Biophys.* **28**, 171-193 (1995).

[S21] P. C. Humphreys, M. Barbieri, A. Datta, and I. A. Walmsley, Quantum enhanced multiple phase estimation, *Phys. Rev. Lett.* **111**, 070403 (2013).

[S22] T. Juffmann, S. A. Koppell, B. B. Klopfer, C. Ophus, R. M. Glaeser, and M. A. Kasevich, Multi-pass transmission electron microscopy, *Sci. Rep.* **7**, 1699 (2017).